Article
journal of Studies of Earth's Deep Interior
doi:10.46298/jsedi.15883

Evidence of a ULVZ near Vanuatu from Sdiff postcursors

Carl Martin * [1], **Lobke Harmsma** [1], **James Atkins** [2], **Arwen Deuss** [1], **Sanne Cottaar** [2]

[1]Department of Geosciences, Utrecht University, 3584 CB, Netherlands, [2]Bullard Laboratories, Department of Earth Sciences, University of Cambridge, CB3 0EZ, UK

Author contributions: *Conceptualization*: CM. *Methodology*: CM, SC. *Software*: CM, SC. *Validation*: CM, LH, JA. *Formal Analysis*: CM, LH, JA, SC. *Investigation*: CM, LH, JA, SC. *Resources*: AD, SC. *Writing - Original draft*: CM, LH. *Writing - Review & Editing*: CM, LH, JA, AD, SC. *Visualization*: CM, LH. *Supervision*: AD, SC. *Project administration*: AD, SC. *Funding acquisition*: AD, SC.

Abstract Thin anomalous structures known as ultra-low velocity zones (ULVZs) have been found on the core-mantle boundary (CMB) and have extreme velocity reductions. These features are detected due to their effect on seismic waves that travel through them, typically producing precursors or postcursors. In this study we use postcursors to shear core-diffracted waves (Sdiff+) that sample the CMB near Vanuatu to detect and characterise the properties of a ULVZ. We identified a total of 19 earthquakes originating from the South Pacific Rise region detected by stations across East Asia – particularly Japan – showing Sdiff+ signals. Of these events, six with the highest quality Sdiff+ signals are included in a Bayesian inversion of travel times using the 2D Wavefront Tracker we previously developed. A subset of events was selected for further analysis by modelling using 3D full waveform synthetics for a range of parameters. The comparison of the real data with the synthetic waveforms suggests that a ULVZ is located to the southeast of Vanuatu at $172.2 \pm 0.9°$ E and $22.9 \pm 1.1°$ S and its broad-scale structure can be approximated as a cylinder with a height of 20 ± 5 km, radius 240 ± 50 km, and shear wave velocity reduction of $30 \pm 5\%$. These parameters are comparable to other ULVZs previously detected and modelled with Sdiff and Sdiff+. There are appreciable uncertainties in the location along the NW-SE direction due to the distribution of earthquakes and seismic arrays, as well as trade-offs between the height, size and velocity reduction of the ULVZ. Other studies using SPdKS, ScP and PcP have reported detections of ULVZs in the proximate region, some of which are consistent with the well-fitting parameter space of the ULVZ in this study. The Vanuatu ULVZ lies within the southwest edge of the Pacific large low velocity province. There is potentially a mantle plume rooted by this ULVZ that has diverted towards the hotspots on the eastern Australian plate around the Tonga slab, although most tomographic models do not show a continuous plume here.

Handling Editor: Vernon Cormier
Received: June 16, 2025
Revised: October 3, 2025
Accepted: October 7, 2025
Published: October 16, 2025

Key points

- We present new evidence for an ultra-low velocity zone (ULVZ) on the CMB to the southeast of Vanuatu using Sdiff postcursors (Sdiff+) from earthquakes in the South Pacific Rise region towards seismic arrays in East Asia.
- The data are broadly explained by a quasi-cylindrical ULVZ located at $172.2 \pm 0.9°$ E and $22.9 \pm 1.1°$ S with height 20 ± 5 km, radius 240 ± 50 km, and shear wave velocity reduction $30 \pm 5\%$.
- Combined with previous studies using ScP and SPdKS in the area, this is a broad-scale region with a patchwork of ULVZs comparable in variety to Hawaii.
- The Vanuatu ULVZ lies within the Pacific large low velocity province, and might potentially be a root to a mantle plume that deflected towards the eastern Australian hotspots around the Tonga slab.

*Corresponding author: c.d.martin@uu.nl

1 Introduction

The lowermost mantle above the core-mantle boundary (CMB) contains strong laterally heterogeneous seismic structures not observed in the rest of the lower mantle (e.g. Ritsema et al., 2011; French and Romanowicz, 2014). Around 30% of the CMB is covered by two large regions with relatively low shear wave velocities, called large low velocity provinces (LLVPs), which are broadly located beneath the Pacific and Africa (e.g. Cottaar and Lekic, 2016; Garnero et al., 2016). The LLVPs have been seen in tomographic models for over 40 years (Dziewonski and Anderson, 1981), with their detailed structure increasing with time (e.g. Thrastarson et al., 2024; Cui et al., 2024). Whether they are thermal plume clusters or thermochemical structures related to superplumes or stable piles is still a subject of debate (e.g. Garnero et al., 2016; Lau et al., 2017; Koelemeijer et al., 2017; Talavera-Soza et al., 2025), although a potential consensus image is emerging of a thin higher density stable base with bundles of thermochemical plumes above (Richards et al., 2023; Davaille and Romanowicz, 2020).

Besides LLVPs, smaller and thinner structures have been identified on the CMB. These structures – known as ultra-low velocity zones (ULVZs) – have much higher shear wave velocity reductions, on the order of 10–50% (e.g. Yu and Garnero, 2018; Li, Leng, et al., 2022). ULVZs have been detected since the mid-1990s using various seismic phases that interact with the CMB (Williams et al., 1998) and are reported to have a broad variation in size (from a few to 100 km in height and a few to 1000 km in lateral extent) and velocity reduction (e.g. summary by Yu and Garnero, 2018). Naturally, there are strong trade-offs between height, size and velocity reduction. ULVZs detected by bounce point phases (ScS, ScP, PcP) or by scattering (PKP) generally lack constraints on their lateral extent or shape, whereas those detected by diffracted phases (Sdiff, SPdKS) sample large portions of the CMB but there are ambiguities in where along those paths anomalies originate. In cases where there is crossing data and/or broad coverage of an area, 3D models of these structures have been proposed. For example, synthetic modelling of rectangular or amorphous shapes for the Samoa mega-ULVZ have been effective in reproducing observed SPdKS data (Thorne et al., 2013; Jensen et al., 2013; Krier et al., 2021). For Sdiff waveforms, cylindrical shapes are typically assumed as they reproduce the observed out-of-plane postcursor signals; including ULVZs found near Hawaii (Cottaar and Romanowicz, 2012; Li, Leng, et al., 2022), Iceland (Yuan and Romanowicz, 2017), Galapagos (Cottaar et al., 2022), Pitcairn (Li et al., 2024), St Helena (Davison et al., 2024) and in the central Pacific (Kim et al., 2020; Wolf and Long, 2023; Martin et al., 2024). With good data coverage for the Hawaii ULVZ, an elongated or elliptical cylinder has been constrained (Li, Sun, et al., 2022; Martin et al., 2023b). These broadest ULVZs of 500–1000 km or more in lateral extent are sometimes referred to as 'mega-ULVZs' (Thorne et al., 2013).

Since ULVZs are relatively thin structures that lie on the CMB, studies are typically focussed on a target region, rely on dense seismic arrays, and mainly use forward modelling to interpret the seismic observations. The first studies to invert for ULVZ morphology investigated layered structures in the radial direction using Bayesian methods to explain pre- and postcursors in ScP waveforms (Pachhai et al., 2015; Pachhai et al., 2023). For Sdiff postcursors (Sdiff+), Martin et al. (2023a) developed a Bayesian method mapping the structure in the 2D horizontal plane, using a wavefront tracker as the forward model (Hauser et al., 2008). These methods illustrate the range of models that can fit the data and reduce the exploration required through forward modelling.

Major questions remain as to what ULVZs are made of and how they form. A chemically distinct composition that is enriched in iron-rich ferropericlase could explain the observed velocity reductions (e.g. Wicks et al., 2010; Dobrosavljevic et al., 2019; Esdaille and Chen, 2024). Geodynamic modelling suggests ULVZs have a composition with a major increase in density, implying that ULVZs have a solid-state origin (Bower et al., 2011). Chemical anomalies have been suggested to be a remnant of a basal magma ocean (Labrosse et al., 2007) or sediments from the outer core (Fu et al., 2023). The presence of partial melt has also been suggested to explain high dVp/dVs ratios (e.g. Williams et al., 1998). Melting of subducted slab material has been proposed to explain ULVZs located in subducted slab regions (e.g. Festin et al., 2024; Li, 2023). However, it is unlikely that the melt will remain stable within the ULVZ over long timescales as it will pool on the CMB, resulting in a global melt layer (e.g. Hernlund and Tackley, 2007; Dannberg et al., 2021), unless there is sufficient internal stirring (Hernlund and Jellinek, 2010). Such a global melt layer has not yet been detected unambiguously due to the seismic resolution limit, but a global layer of up to several kilometres may be possible (e.g. Russell et al., 2022; Hansen et al., 2023). Longer period normal modes are also consistent with a thin global layer (Russell et al., 2023) but alternatively this could be due to a long wavelength component in the distribution of piled ULVZ material (Koelemeijer et al., 2012).

Besides their nature, their relationship with surrounding flow remains unknown. Some studies have suggested a relationship between mega-ULVZs and hotspots at the surface and potential mantle plumes connecting them (Thorne et al., 2013; Yuan and Romanowicz, 2017; Kim et al., 2020; Cottaar and Romanowicz, 2012), which is consistent with geophysical models (e.g. Jellinek and Manga, 2002). ULVZs might therefore represent a reservoir to explain anomalous signatures of $^{3}He/^{4}He$ and $\mu^{183}W$ (Mundl-Petermeier et al., 2020; Cottaar et al., 2022). However, anomalous geochemical observation are not always observed at plumes near ULVZs (Herret et al., 2023; Davison et al., 2024), nor can all mega-ULVZs be related to a hotspot or mantle plume (Martin et al., 2024). The latter is particularly true for the large range of smaller ULVZs that are observed globally (e.g. Yu and Garnero, 2018; Hansen et al., 2023). The largest observed ULVZs are also predominantly located at the boundaries of the LLVPs, which is consistent with geodynamical modelling that suggests that dense ULVZs that form outside the LLVPs are swept to the boundaries and accumulate there (Liu et al., 2024).

In this study, we focus on the region of the CMB beneath the Southwest Pacific, near Vanuatu and Fiji. Positive detections and null observations of ULVZs have been reported here from multiple seismic probes (Yu and Garnero, 2018) (summarised in Figure 1). Due to the distribution of earthquakes caused by the subduction of the Pacific plate under the Australian plate with respect to the Alice Springs and Warramunga seismic arrays in Australia, there are numerous studies which have investigated the structure of ULVZs in this region using ScP waveforms (e.g. Rost and Revenaugh, 2001; Idehara et al., 2007; Brown et al., 2015; Pachhai et al., 2015). Using the same events, other studies have investigated the possibility of ULVZs here from anomalous SPdKS waveforms (e.g. Thorne and Garnero, 2004; Jensen et al., 2013; Thorne et al., 2021).

The wide range of reported parameters and locations for a possible ULVZ indicate that substantial uncertainty remains regarding the fine-scaled structures on the CMB in the New Caledonia/Vanuatu region.

Here, we present new observations of Sdiff postcursors (Sdiff+) which sample the CMB and provide evidence of a ULVZ in the region beneath Vanuatu and Fiji, from earthquakes in the Pacific Rise region towards stations across East Asia. We thus refer to the ULVZ causing these Sdiff+ signals as the 'Vanuatu' ULVZ. We invert for ULVZ location and parameters from Sdiff+ travel times with a 2D wavefront tracker for six high quality events. From the ensemble of models which fit the data we compute 3D full waveform synthetic models for several of the highest quality events to test

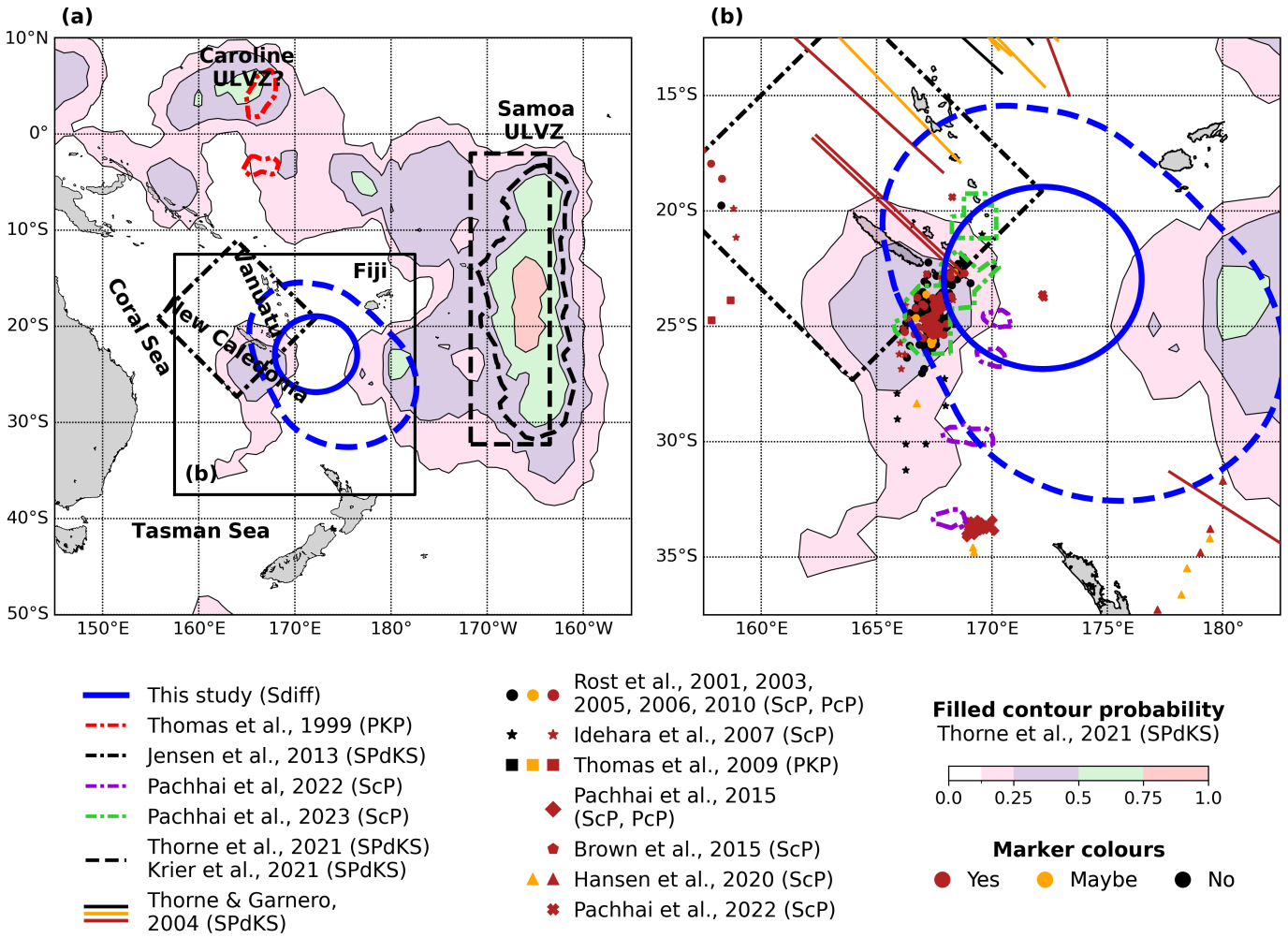

Figure 1: (a) Probability map of the presence of ULVZs based on the 1% misfit map by Thorne et al. (2021). Note that there is no distinction in this study between low probability and poor data coverage. The dashed black line is the Samoa ULVZ from Thorne et al. (2021) and Krier et al. (2021). The black dashdotted line gives the proposed ULVZ from Jensen et al. (2013). The dashed blue line represents the convex hull of our well-fitting parameter space of the ULVZ found in this study. The solid blue line gives the preferred model of the ULVZ in this study, with a radius of 240 km and location 172.2° E and 22.9° S. (b) Zoom-in of the black box in (a) with locations of bounce points on the CMB given by: circles (Rost and Revenaugh, 2001; Rost and Revenaugh, 2003; Rost et al., 2005; Rost et al., 2006; Rost et al., 2010), stars (Idehara et al., 2007), squares (Thomas et al., 2009), diamonds (Pachhai et al., 2015), pentagons (Brown et al., 2015), triangles (Hansen et al., 2020), and crosses (Pachhai et al., 2022). The lines are ray paths of SPdKS waveforms on the CMB from Thorne and Garnero (2004). Their colours indicate the presence (red) and absence (black) of anomalous waveforms; complex waveforms (orange) are not interpreted. The coloured dashdotted lines are proposed ULVZs in the region surrounding Vanuatu from multiple previous studies (Thomas et al., 1999; Thorne et al., 2013; Pachhai et al., 2022; Pachhai et al., 2023).

constraints on the thickness, lateral extent, and shear wave velocity reduction of the ULVZ. Finally, we go on to compare our model with others reported in this region, which are largely consistent.

2 Data and Methods

2.1 Sdiff postcursors (Sdiff+)

Shear waves diffract along and propagate parallel to the CMB and can be observed beyond epicentral distances of approximately 100° (Sdiff, Figure 2a), although this varies depending on the assumed 1D velocity model and event depth. Energy of the Sdiff wave gets trapped and propagates as a guided wave within the ULVZ, lagging behind energy of the Sdiff waves propagating above or around the ULVZ. Due to the velocity contrast at the boundaries of the ULVZ, the guided wave is also refracted upon entry and exit of the ULVZ. As a result, the propagation of the wavefront is disturbed and creates postcursors to the main Sdiff phase (Figure 2b), here referred to as Sdiff+. The time delay of the Sdiff+ compared to the direct Sdiff phase is caused by both the propagation within the ULVZ and the longer path taken due to refraction when off-axis. Sdiff+ signals caused by a cylindrical ULVZ have an approximately hyperbolic travel time moveout, with the minimum arrival time at the on-axis azimuth relative to the ULVZ midpoint from the source.

Detection of Sdiff+ requires a large and dense seismic array. In particular, most recent studies of ULVZs using Sdiff+ have only been possible due to the dense coverage of seismic stations in North America (e.g. Cottaar and Romanowicz, 2012; Yuan and Romanowicz, 2017; Cottaar et al., 2022; Wolf and Long, 2023; Martin et al., 2024), while some Sdiff+ signals have been observed by networks throughout Europe (Davison et al., 2024), central Asia (Yuan and Romanowicz, 2017), and South America (Li et al., 2024). Here, we use a

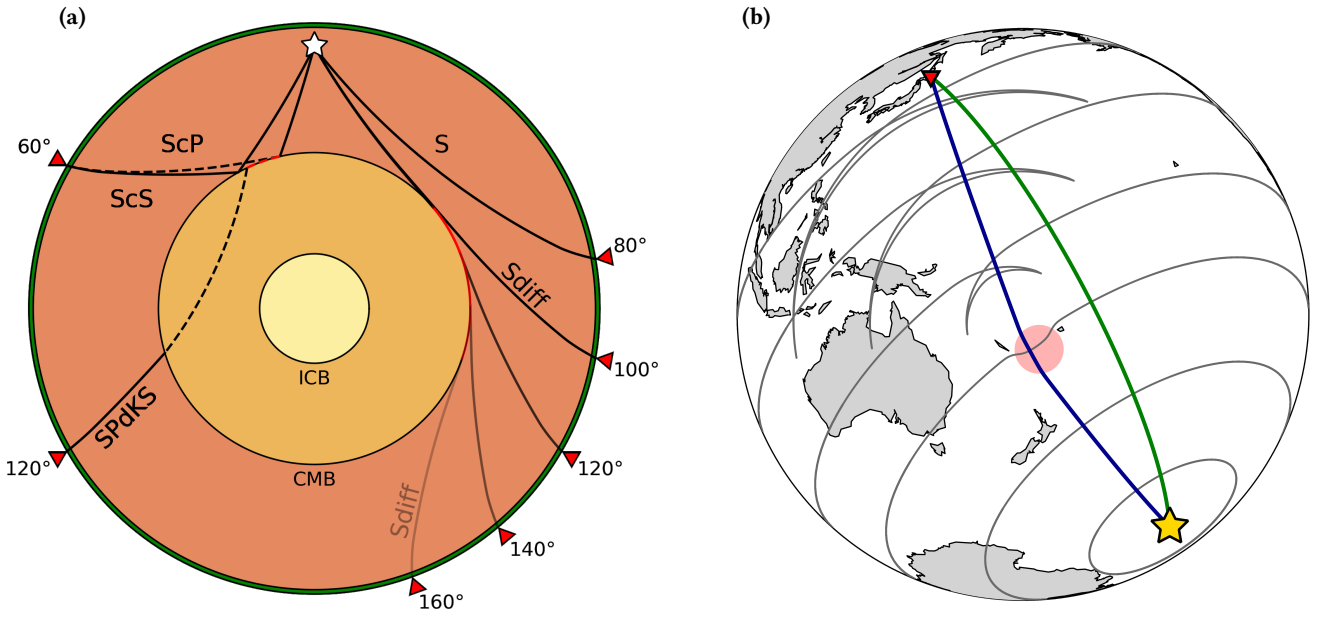

Figure 2: (a) Propagation of ScP, ScS, SPdKS, S, and Sdiff seismic phases from an earthquake (star) to receivers (triangles) through a cross-section of the Earth. ScP and ScS are core-reflected phase that sample bounce points on the CMB. SPdKS and Sdiff are phases that have diffracting legs along the CMB, with diffraction ray paths that attenuate with distance. (b) Wavefront propagation of Sdiff from an earthquake (star), calculated using the 2D wavefront tracker (Hauser et al., 2008; Martin et al., 2023a). The wavefront propagates through time (sequential grey lines), producing postcursor signals as it passes across a ULVZ (pink circle). A receiver (triangle) detects the direct arrival (Sdiff, green line) and an additional delayed arrival due to refraction from the ULVZ (Sdiff+, blue line) at a different angle to the direct backazimuth.

new geometry from the South Pacific Rise to stations in East Asia.

In this study, Sdiff specifically refers to SHdiff, observed on the transverse component, which is observable at epicentral distances up to 150° for sufficiently large earthquakes. SVdiff, on the other hand, is strongly attenuated in the diffracted portion due to leaking into the core, resulting in a large decay in amplitude as a function of epicentral distance (Komatitsch et al., 2010) and is not studied further here.

2.2 Data selection

We search for evidence of Sdiff+ for events in the South Pacific Rise region using the dense seismometer distribution in East Asia. We inspected all earthquakes located near the South Pacific Rise region at any depth from 1995 to 2024 and with a moment magnitude larger than 5.5. Data are obtained for a distance range of 90–150°, although most data in this geometry is observed at 115–130°.

The seismograms were downloaded from networks available through the EarthScope Consortium Data Management Center and the National Research Institute for Earth Science and Disaster Prevention (hereafter NIED) F-net, a broadband seismograph network consisting of more than 70 stations across Japan (Okada et al., 2004). After downloading, the data were resampled to 10 Hz, components checked for missing data, and rotated into the ZRT (vertical, radial, tangential) orientation since SHdiff is primarily visible on the tangential component.

A total of 78 earthquakes located in the South Pacific Rise region were analysed. Most of the earthquakes had a low signal-to-noise ratio (SNR) due to their low moment magnitude. There were 19 earthquakes with sufficiently high SNR, all of which showed Sdiff+ signals (Table S1, Figure 3). From this catalogue, a total of six earthquakes with the most prominent Sdiff+ signals were chosen for modelling (Table 1). For these six events, individual seismograms with a low SNR (by visual assessment) were removed. The waveforms of the six earthquakes are shown in Figure 4, with the interpreted postcursors highlighted. Since Events 4a & 4b are nearly co-located they are plotted in the same subplot. For Events 2 & 3, the postcursor move-out can only be identified on one side, which is likely due to station distribution, an effect of the source, or both.

Since Sdiff ray paths sample a large distance along the CMB, an anomaly anywhere along that path may have caused the Sdiff+. To obtain a constraint on the location of the ULVZ with better accuracy, it is important to have source-receiver paths that sample the CMB from different directions. To complement our data set, we investigated events with alternative source-receiver geometries, but we observed no unambiguous Sdiff+ signals. For events in New Zealand and Macquarie Island towards Alaska, the ULVZ near Hawaii – which produces high amplitude Sdiff+ signals (e.g. Martin et al., 2023b) – is in the sampling region, so any signal of the Vanuatu ULVZ cannot be easily distinguished. For events in Russia or West Alaska towards Antarctica, the distance range of 140–150° is challenging, and data is generally noisy, resulting in low SNR for most events. There are some very large earthquakes for which SNR is relatively good, but the source mechanisms are complex. Combined with the poor station coverage here, the data are difficult to interpret. As a result, we only sample the CMB near Vanuatu along one general direction, with only Events 1 & 2 providing a slightly different angle from the other four events (Figure 3).

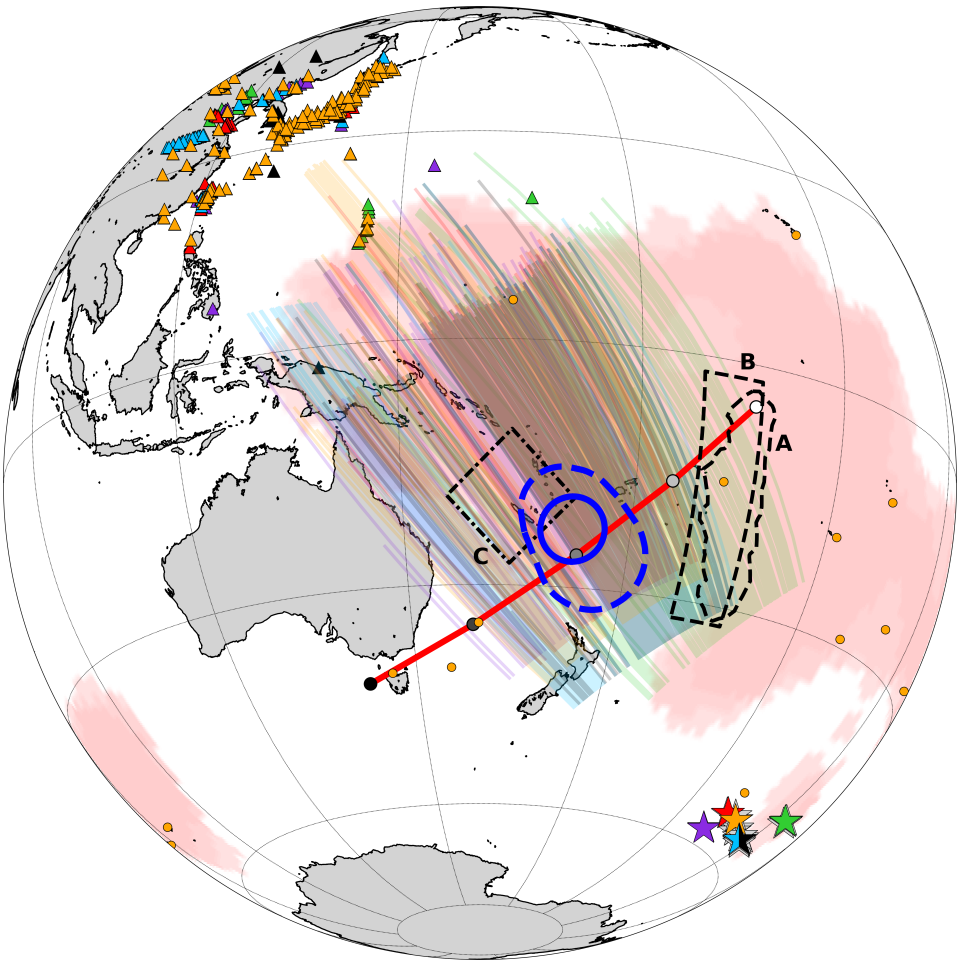

Figure 3: Map of event locations (stars), receivers (triangles) and the Sdiff ray paths sensitive to the CMB (below 2800 km depth). The earthquakes and ray paths are coloured per event: 1–green, 2–purple, 3–red, 4a–blue, 4b–black and 5–orange (Table 1); light grey stars are events identified but not analysed (Table S1). Hotspot locations are shown as orange circles. The dashed blue line represents the convex hull of ensemble of models of ULVZs which fit the Sdiff+ arrival time data in this study. The solid blue line gives the preferred model of the ULVZ in this study, with a radius of 240 km and location 172.2° E and 22.9° S. The models of the Samoa ULVZ are given as black dashed lines: A–irregular shaped (Thorne et al., 2021) and B–rectangular shaped (Krier et al., 2021). The black dashdotted line shows the inferred C–diamond shaped ULVZ from Jensen et al. (2013). The background displays the LLVP vote map at 2800 km depth (Cottaar and Lekic, 2016). The solid red line and greyscale markers denote the cross-section transect in Figure 8.

2.3 Data set

The same set of waveforms for the six events in Figure 4 are shown for 7–12, 20–30 and 30–40 s period bands in Figures S1–S3, respectively. The Sdiff+ signals have low SNR at higher frequency but coherent waveforms are still visible in Events 1, 4a and 4b where there is densest ray coverage. At lower frequency the postcursor signals are subtle but still visible. With the caveat that these events are all shallow and observed at relatively long epicentral distances (115–130°), the frequency content of Sdiff+ waveforms is comparable to that observed for the Hawaii ULVZ, and extends to lower frequencies than observed for Iceland or the mid-Pacific ULVZs (Martin et al., 2024).

As well as the network of broadband seismometers – F-net – NIED also operate a network of approximately 700 short period seismometers – Hi-net – with a dominant period of 1 s and an average station spacing of 20 km (Okada et al., 2004). We downloaded and processed the data in the same way as previously described but only for the six events in Table 1. Despite the dominant period of the Sdiff+ being outside the corner frequency of the instruments, the postcursors are still clearly visible in the data filtered between 7–12 and 10–20 s period (Figures S4 & S5). The signal is noticeably more apparent in the linear stack of each azimuthal bin. Since this data set is only available for mainland Japan, the azimuthal coverage is narrow which makes it unsuitable for inclusion in our analysis. Nonetheless, it acts as a promising demonstration for the use of short period seismometers to detect ULVZs with phases of characteristically longer periods in future studies.

For several events, the Sdiff+ signals exceed the amplitudes of the main Sdiff signals. This effect is especially noticeable for Events 3–5 in the broadband (Figure 4) and short period instrument data (Figure S4). Weak or non-apparent Sdiff has also been previously observed in events from New Zealand to Alaska for the Hawaii ULVZ (Martin et al., 2023b), which might suggest that ULVZs have a strong focussing effect on data which may amplify or preserve the postcursor signal.

2.4 Inverse modelling

We first explore the likely location and size of the ULVZ using a reversible jump Markov chain Monte Carlo inversion

	Date	Longitude (°)	Latitude (°)	Depth (km)	Magnitude	Time shift (s)	Region
1	2003/08/28	-115.20	-49.92	15	6.2	-5.0	Southern East Pacific Rise
2	2005/05/12	-138.91	-57.57	12	6.5	-3.0	Pacific-Antarctic Ridge
3	2001/09/02	-136.75	-54.31	15	6.3	0.0	Pacific-Antarctic Ridge
4a	2007/03/31	-123.61	-55.94	12	6.2	-9.5	Southern East Pacific Rise
4b	2016/08/18	-123.63	-55.97	13.44	6.0	-9.5	Southern East Pacific Rise
5	2015/05/19	-132.39	-54.53	14.91	6.6	-1.5	Pacific-Antarctic Ridge

Table 1: List of selected events with high quality Sdiff+ signals. Source parameters are from the Global CMT Project (Ekström et al., 2012). The full list of events can be found in Table S1.

setup (rj-McMC). To perform the forward modelling, we use the 2D Wavefront Tracker (2DWT), originally developed by Hauser et al. (2008) and adapted to the CMB by Martin et al. (2023a), to model the Sdiff+ arrival times of a ULVZ on the CMB in a matter of seconds. We disregard the up- and downgoing parts of the Sdiff path in this approach. An example of wavefronts computed by 2DWT is shown in Figure 2b. The parametrisation of the model is a circle that can change in location or in size and velocity reduction. In the case of Hawaii, where crossing data was available, we also included ellipticity (and rotation) as parameters (Martin et al., 2023b), but in the case of the central Pacific ULVZ (Martin et al., 2024) and here, we limit our model to a single circle in order to reduce the parameter space. We run 100 chains in parallel and then sparsely sample each chain after a burn in period. The resulting ensemble of models is assumed to be representative of the posterior distribution and demonstrates the trade-offs between position, size and velocity of the ULVZ models which fit the data (e.g. Bodin and Sambridge, 2009). Further details for the method and various tests can be found in Martin et al. (2023a).

We invert for observed travel time delays of the Sdiff+ with respect to the predicted arrival time of Sdiff with a correction for each event. In Martin et al. (2023a) we extracted Sdiff+ arrival times by cross-correlating synthetics for a 1D model with the observed data.

However, as the observed data across the azimuth ranges have a very similar Sdiff waveform shape, we simply take the arrival times of the Sdiff+ as the continuous peak of the waveform maximum as highlighted in Figure 4. Note that the data plotted are time shifted by the values in Table 1 in order to align the Sdiff arrivals, which is necessary due to the delay caused by the presence of the LLVP along the paths besides uncertainty in the source. The travel time picks are plotted in Figure 5c.

This inversion gives us an initial estimate of the trade-off between velocity reduction and imprint of the ULVZ on the core-mantle boundary, but full waveform modelling is still required to determine its height and further trade-offs.

2.5 Forward modelling

We use AxiSEM3D (Leng et al., 2019) to compute synthetic waveforms for 3D ULVZ models, with isotropic PREM as the 1D background model. A discontinuity at the height of the ULVZ above the CMB is added to force the mesh to include a sharp change in velocity at the ULVZ top. AxiSEM3D uses a 2D mesh, with sampling accuracy in the third dimension being specified by the number of terms included in the Fourier expansion at each mesh point, referred to as the *Nr* field. We use a custom *Nr* field to lower the required azimuthal complexity in regions unaffected by our ULVZ model (e.g. epicentral distances closer than the ULVZ or beyond the furthest station) to reduce computational cost at minimal expense to accuracy (Russell et al., 2025).

The range of parameters of the ULVZ for 3D modelling are taken from the result of the rj-McMC inversion of Sdiff+ arrival times. The circular anomaly in 2D is modelled as a cylindrical structure in 3D, and a range of heights are tested from 15 to 30 km. We also test a range of velocities and sizes to illustrate the trade-offs in full waveform synthetics.

For each model, the pressure wave velocity and density are both unchanged relative to PREM, as these choices minimally affect the SHdiff waveforms (Cottaar and Romanowicz, 2012). The waveforms across the events are fairly similar (after flipping the polarity for Event 2). However, we found the moment tensors from the Global CMT Project catalogue (Ekström et al., 2012) do not fit the observations well. We compared the data to synthetics calculated using Instaseis (Driel et al., 2015) for a range of event depths from 0–50 km. We found that a depth of 0 km resulted in the most consistent match for Sdiff (main arrival) waveforms between the data and synthetics calculated with PREM (Figure S6).

3 Results

3.1 Inverse modelling

We first make an initial estimate of the location, size and velocity reduction of the ULVZ using our rj-McMC method (see Section 2.4). The resulting sparsely sampled distribution of 100 separate chains, drawn after a burn in period, is taken to be representative of the posterior distribution of the ULVZ parameters (Figure 5a-b). As the observations are roughly from a single direction, there is still a wide range locations and size/velocity values in the final ensemble. The locations of the models show a larger uncertainty in the NW-SE direction and smaller uncertainty in the SW-NE direction, but the posterior distribution suggests a single pronounced peak (Figure 5a). There is no preferred model for the trade-off between velocity reduction and size (Figure 5b), although there does appear to be a trade-off with location: models centred further north-east prefer a larger weaker anomaly than those further south-west.

The median parameters of the ensemble for an inversion with a circular anomaly are: radius 230 ± 50 km and velocity reduction of $31 \pm 5\%$ with respect to PREM at the CMB, centred at $172.2 \pm 0.9°$ E and $22.9 \pm 1.1°$ S. Computed arrival times for the median parameters show general agreement with the observed arrival times (Figure 5c), but we note that these are not necessarily the parameters which minimise the misfit with the data.

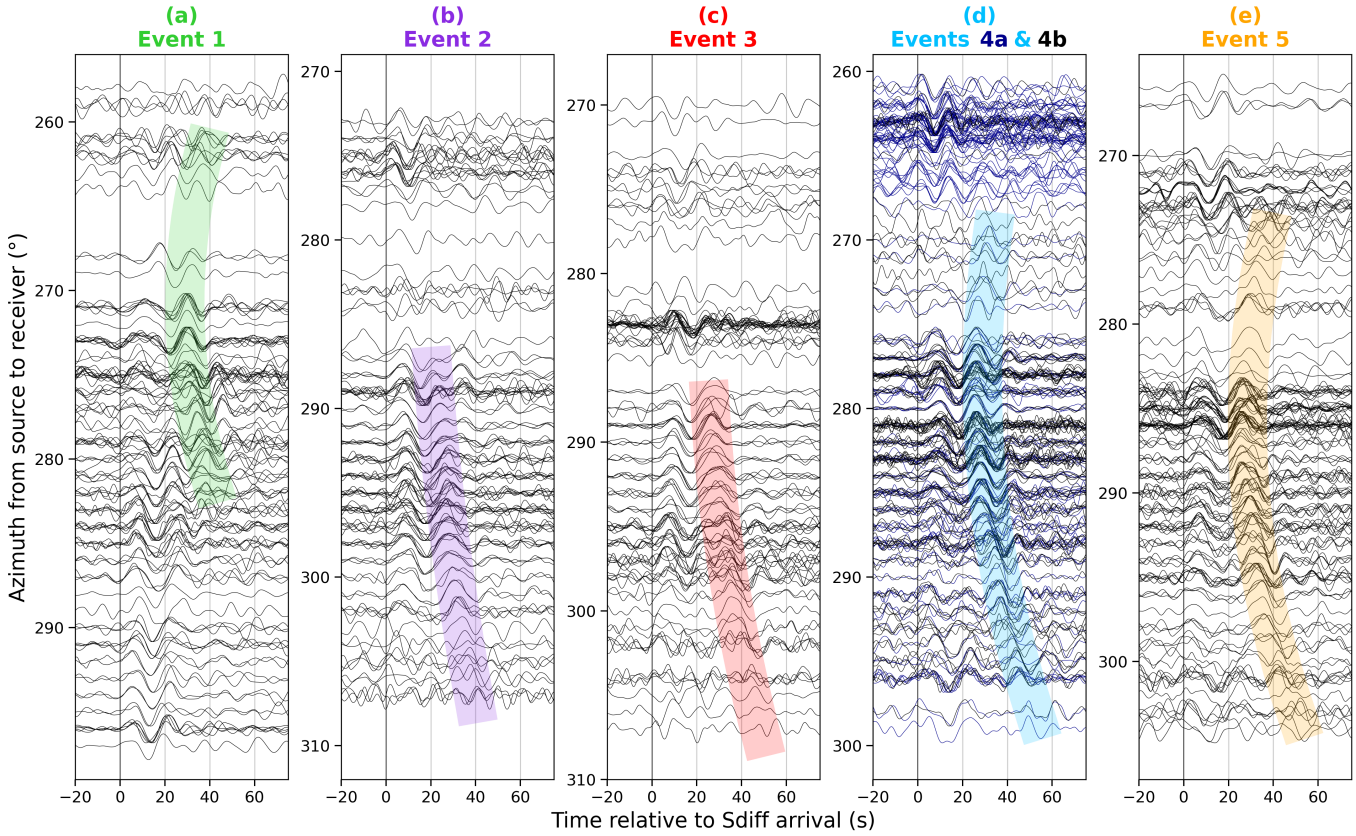

Figure 4: Displacement waveforms on the transverse component filtered between periods of 10–20 s for the six events listed in Table 1. The waveforms are plotted as a function of azimuth (rounded to the nearest integer). The data are plotted with respect to the predicted Sdiff arrival time calculated from the Preliminary Reference Earth Model (PREM, Dziewonski and Anderson, 1981) using the TauP toolkit (Crotwell et al., 1999), adding a constant overall shift for each event up to 10 seconds to shift the reference phase to the predicted arrival time as we expect a shift due to uncertainty in event location and the presence of the LLVP. The shifts applied to each event are included in Table 1. Events 4a (dark blue) & 4b (black) are co-located and plotted together. The Sdiff+ are highlighted, and the colours correspond to the event location stars in Figure 3. Note that the waveforms for Event 2 have been flipped.

We proceed to model the anomaly with 3D full waveform synthetics for a cylinder centred at the median location with a range of parameters to assess the trade-offs between size and velocity reduction with height, for which the 2DWT inversion cannot provide any insight.

3.2 Forward modelling

In this section, we compare the data to 3D full waveform synthetics (see Section 2.5) for a number of models to demonstrate the trade-off in parameter space between height, radius and velocity reduction for a cylindrical ULVZ. The parameter combinations considered are chosen to represent the observed trade-off between radius and velocity reduction in the 2DWT inversion for a circular anomaly (circles in Figure 5b).

3.2.1 Constraints on height

For Events 4a & 4b, we compute synthetics for a cylindrical model of 30% shear velocity reduction and 240 km radius, close to the median values from the inversion, and for a range of heights: 15, 20, 25 and 30 km. A ULVZ thinner than 15 km would not be expected to have visible Sdiff+ between 10–20 s (Martin et al., 2024). Observing when the Sdiff+ is visible in the synthetic data when filtered between period bands 10–20 and 20–30 s allows us to estimate the height of an approximate cylindrical model (Figures S9 & S10). There remains some ambiguity in this trade-off due to the fixed values of velocity reduction and size; however, the lack of visibility of Sdiff+ in the data at longer periods suggests 30 km is too thick. We therefore continue with further modelling with a height of 20 km, but acknowledge a significant uncertainty of ±5 km.

3.2.2 Constraints on shear velocity and size

Synthetics for parameters along the size-velocity trade-off curve for the 2DWT inversion ensemble (Figure 5b; Models A1–A5 in Figure S7 & Table S2) all result in Sdiff+ which more or less follow the same arrival time move-out curve (Figures S11 & S12), validating the result of the 2DWT inversion. However, there is significant variation in the relative amplitudes between Sdiff and Sdiff+, with small but strong anomalies resulting in small Sdiff+ amplitudes, and large but weak anomalies producing large Sdiff+ amplitudes.

We also compute synthetics for models away from the trade-off curve to demonstrate the unsuitability of these models and illustrate uncertainties. A number of tested models are larger or more strongly reduced (Models B1, B3 & C1; 'above' the curve in Figure S7), resulting in pronounced Sdiff+ that are more delayed and have longer periods than observed in the real data (Figures S13 & S14). For models that are smaller or more weakly reduced (Models B2, B4 & C2;

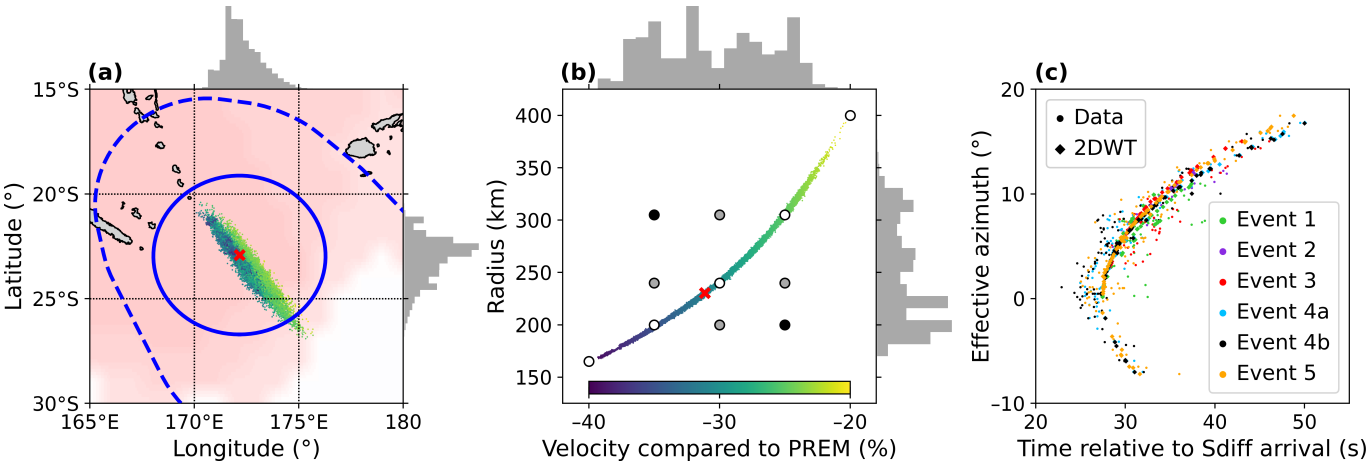

Figure 5: Ensemble of models that fit the Sdiff+ arrival times from the rj-McMC, showing the distribution of (a) midpoint locations and the (b) trade-off in ULVZ velocity reduction and radius. The median model is marked with a red cross and histograms of each of the parameters are projected onto the respective axes. The outline of the median model (~230 km radius and ~31% velocity reduction, located at 172.2° E and 22.9° S) and convex hull of the ensemble parameter space are shown as solid and dashed blue lines, respectively (the full convex hull can be seen in Figures 1 & 3). Colours of model midpoints in (a) correspond to the velocity value of the ensemble model, which approximately corresponds to radius. The background in (a) corresponds to the LLVP vote map at 2800 km depth (Cottaar and Lekic, 2016). Circles in (b) are parameters used for full waveform modelling of trade-offs (Figure S7 & Table S2). (c) Comparison of the Sdiff+ arrival times and the predicted data for the median model. Predicted arrival times for all models in (b) are shown in Figure S8.

'below' the curve in Figure S7), the Sdiff+ are comparable in amplitude when filtered between 10–20 s but are too weak to be observed in 20–30 s. As expected, the travel time delays of the Sdiff+ are reduced. Overall, there are appreciable trade-offs of the size and velocity reduction with the thickness of the ULVZ, which is reflected in the uncertainties in our final preferred model.

3.3 Preferred model

The consistent presence of Sdiff+ arrivals in the observed data is strong evidence for the existence of a ULVZ beneath Vanuatu on the CMB. Inversion of the Sdiff+ arrival times with the 2DWT suggests a ULVZ located at 172.9 ± 0.9° E and 22.9 ± 1.1° S. Further modelling with 3D full waveform synthetics shows the data are consistent with a cylindrical ULVZ with radius 240 ± 50 km, height 20 ± 5 km, and shear wave velocity reduction 30 ± 5%. Synthetics for all of the events used in this study are shown in Figure 6.

Whilst the ULVZ was modelled using a simplified cylindrical shape, which effectively reproduces the hyperbolic move-out of Sdiff+, the limited azimuthal coverage of the region of interest makes it difficult to justify to what extent this approximation is reasonable. As Sdiff travels long distances along the CMB, anomalous structures anywhere along those ray paths may cause interference and produce additional waveforms. The available data set samples the ULVZ along a single azimuth (NW–SE), meaning the location is poorly constrained along the ray paths in the NW–SE direction but well constrained in the NE–SW direction (Figure 5a).

4 Discussion

4.1 Comparison to nearby earlier studies

The Southwest Pacific has been intensively investigated, with previous studies finding evidence of the presence and absence of ULVZs using ScP and SPdKS (summarised in Figure 1). A probability map derived from anomalous SPdKS waveforms suggests the likelihood of ULVZs to the west, north, and particularly to the east of our preferred model location (Thorne et al., 2021), where locally targeted studies have mapped the Samoa ULVZ (Thorne et al., 2013; Krier et al., 2021). To the west, the fortuitous source-receiver distribution has led to a plethora of studies using ScP to probe beneath the Coral Sea (e.g. Idehara et al., 2007; Rost et al., 2010; Pachhai et al., 2022), as well as a localised study using SPdKS (Jensen et al., 2013). Since the analyses of these data assume an in-plane origin of pre- or postcursors in the waveforms, it is possible that out-of-plane energy from the ULVZ identified in this study could cause these signals (Pachhai et al., 2024) and we note that the Vanuatu ULVZ is located in a gap of in-plane data coverage for both phases.

We test if our data would be able to observe the other ULVZs previously proposed in the region by computing full waveform synthetics for Events 1 and 4a & 4b. For the two published Samoa ULVZ models – an irregular shaped ULVZ (Thorne et al., 2021) and a rectangular shaped ULVZ (Krier et al., 2021) – we use a thickness of 26 km and a shear wave velocity reduction of 20% as implemented by Krier et al. (2021). To the west, we test a ULVZ in the region of highest probability (purple contour in Figure 1), which is comparable in size to our preferred model. For this we use parameters from our preferred model with radius 240 km, height 20 km and shear velocity reduction of 30% relocated to the midpoint of the local high probability region, 166° E and 24.5° S. The majority of previous ScP studies in this region therefore fall within the boundaries of this trial model, as well as within the upper limit of uncertainty in radius for our preferred model (Figure S15). All ULVZ models tested produced Sdiff+ signals (Figures S16 & 7 for Events 1 and 4a & 4b, respectively).

For the models of ULVZs to the east, Sdiff+ waveforms are offset significantly to the larger azimuths, which means that the Sdiff+ in the observed data cannot be caused by the Samoa ULVZ (Figure 7d-e). However, this does not exclude the possibility that these contribute to the waveform com-

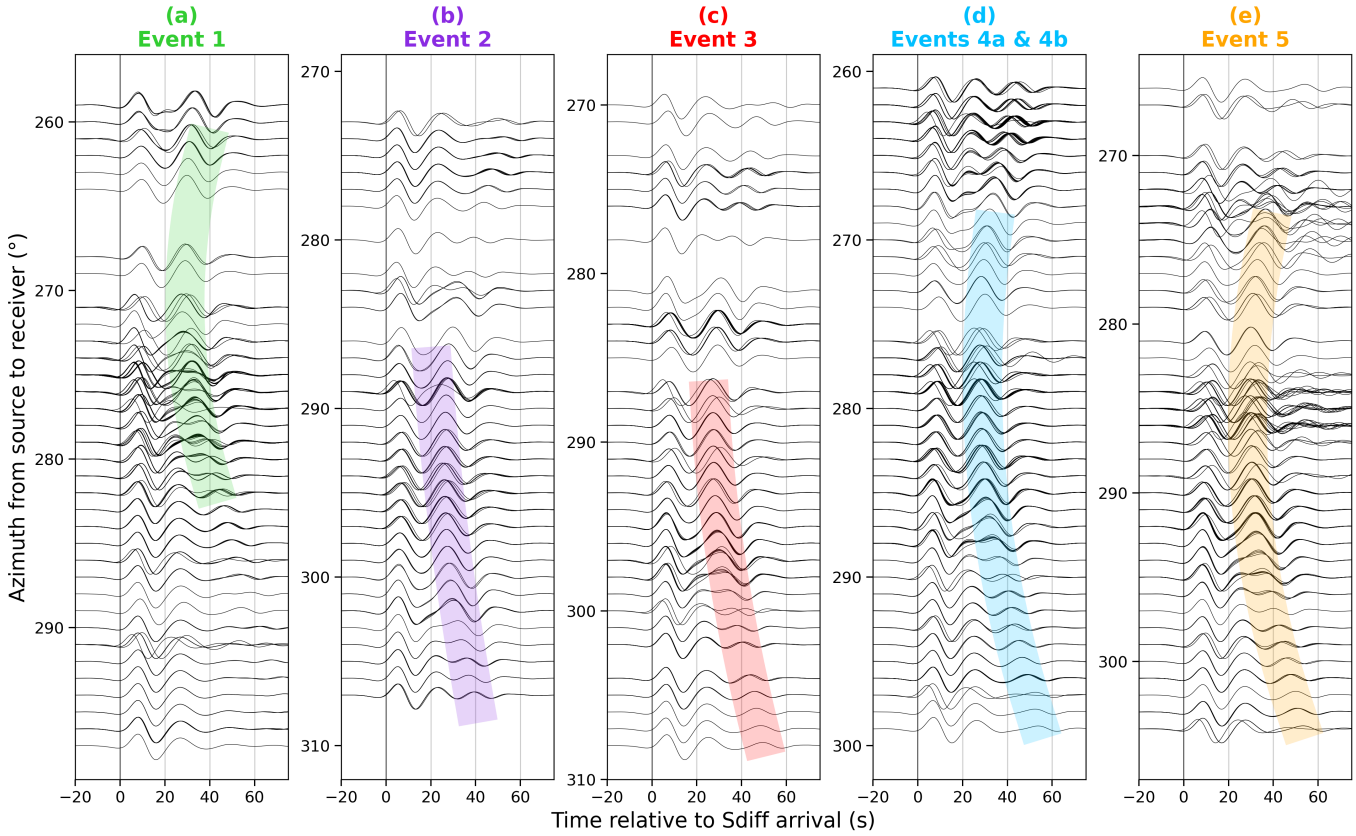

Figure 6: Displacement synthetics for PREM with a ULVZ with height 20 km, radius 240 km, and shear velocity reduction of 30% (Model A3, Table S2) filtered between periods of 10–20 s for the six events listed in Table 1. The same Sdiff+ highlights from Figure 4 are overlaid, and the colours correspond to the event location stars in Figure 3.

plexities observed, nor would lack of signals necessarily contradict the presence of the Samoa ULVZ (Figure S16g), as we have previously noted that the visibility of ULVZs might vary by direction (Martin et al., 2023b). For the model to the west, the waveforms look – perhaps unsurprisingly – fairly similar, as we used the properties of our preferred model, but they are offset to smaller azimuths. While the offset in azimuth is only slight for Event 1 (Figure S16f), it is quite appreciable for Event 4 (Figure 7f). This demonstrates that the location of our preferred model is well constrained by the combination of all six events, each with slightly different coverage, at least in the SW-NE direction.

While a mega-ULVZ model further to the west might not be expected in our data, a range of ScP studies in this region have observations that fall within the convex hull of our model space (Figure 1). These observations from bounce point studies, however, suggest thinner and patchier ULVZ coverage than we infer here (e.g. Idehara et al., 2007; Rost et al., 2010; Pachhai et al., 2022), which could be the narrower edge of a larger, thicker structure (Jensen et al., 2013). Given the low sensitivity of Sdiff and Sdiff+ waveforms to small-scale structures at relatively long period, this study cannot resolve the complex morphology of this regional structure, but supports the presence of a large, thick quasi-cylindrical structure (~500 km across, ~20 km deep). The possibility of in-plane and out-of-plane postcursors caused by a mega-ULVZ should be considered in future studies attempting to reconcile observations of ScP with observations of Sdiff and SPdKS. Overall, this region appears to have many complexities observed by different seismic phases, similar to the patchier areas found around the mega-ULVZ near Hawaii (Jenkins et al., 2021).

Future studies using Sdiff+ and SPdKS could also examine the possible internal layering of ULVZs by using shorter period postcursors. Identifying Sdiff+ at higher frequencies is challenging as they are often obscured by noise, although Li, Leng, et al. (2022) have been able to identify the internal layering of the Hawaii ULVZ using this method.

4.2 Comparison to other mega-ULVZs and relation to LLVPs

The Vanuatu ULVZ has comparable parameters to – but is somewhat smaller in lateral extent than – other modelled mega-ULVZs which have been observed using Sdiff+ (e.g. Cottaar and Romanowicz, 2012; Davison et al., 2024). Since the events sampling this ULVZ are typically shallow and low magnitude, it is difficult to differentiate between weak Sdiff+ signal and noise at shorter periods. There is distinct Sdiff+ energy between 10–20 s period and it is visible up to 30 s, suggesting a comparable frequency content and thickness to that of the Hawaii ULVZ (20 km in height, Martin et al., 2023b) and thicker than that of Iceland (15 km, Yuan and Romanowicz, 2017) or the mid-Pacific ULVZ (10 km, Martin et al., 2024).

At the southwest edge of the Pacific LLVP, the Vanuatu ULVZ is the eighth mega-ULVZ modelled in 3D. All of these – so far – are located at or near the LLVP boundaries, reinforcing a potential correlation between the largest ULVZs and the boundaries of the LLVPs. Previous mega-ULVZs have also been interpreted as whole mantle plume roots due

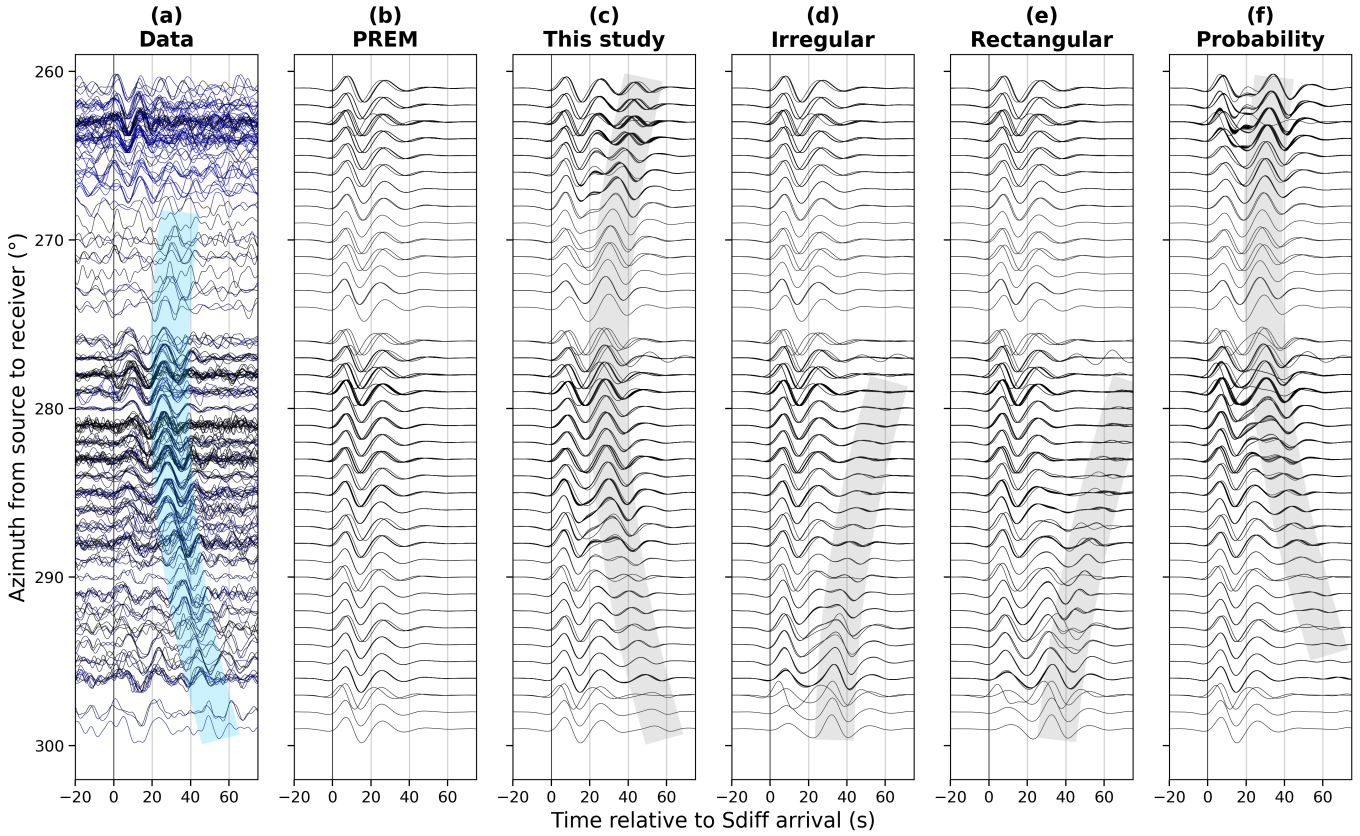

Figure 7: Waveform data and synthetics for the Vanuatu ULVZ in this study and for other models of proximate ULVZs. (a) Observed and (b-f) synthetic displacement waveforms for Events 4a & 4b. Synthetics for PREM with (b) no ULVZ, (c) the preferred ULVZ in this study, (d) the irregularly shaped Samoa ULVZ (Thorne et al., 2021), (e) the rectangular-shaped Samoa ULVZ (Krier et al., 2021), and (f) a ULVZ with parameters of our preferred model centred at the proximate probability peak of Thorne et al. (2021) (Figure S15). The Sdiff+ signals are highlighted where visible. Data are filtered between 10–20 s period.

to their geochemical signatures (Cottaar et al., 2022). The Vanuatu ULVZ is almost equidistant to the Samoa and Lord Howe hotspots, with roughly ~15–20° to either. However, the Samoa ULVZ lies closer to that hotspot and has previously been suggested as its potential root (e.g. Thorne et al., 2013; Krier et al., 2021).

The Lord Howe seamount chain lies on the eastern Australian plate. This seamount chain, combined with the Tasmantid and Eastern Australia hotspot, tracks further west and has no observable topographic swell, implying that the heat flux in the area is very minor (Hoggard et al., 2020). However, the Lord Howe seamount chain has similar geochemical signatures to other Pacific ocean island basalts, with Sr-Nd isotope analysis suggesting a deep mantle source (Rogers et al., 2023). These signals are also seen on the Tasmantid seamount chain suggesting a similar source, but $^{3}He/^{4}He$ measurements to confirm a primordial reservoir are lacking in the region (Rogers et al., 2023).

We show cross-sections for three tomographic models (French and Romanowicz, 2014; Cui et al., 2024; Thrastarson et al., 2024) between the Lord Howe and Samoa hotspots, across the location of the Vanuatu ULVZ (Figure 8). There are differences between the cross-sections, but all three models show the Tonga slab, the Pacific LLVP, and a broad-scale potential plume beneath Samoa, underlain by the Samoa ULVZ. Another, older slab has been suggested in this region at a depth of ~1100 km from a fossil subduction zone (Schellart et al., 2009; Van der Meer et al., 2018). The South Loyalty Basin slab is difficult to distinguish from the Tonga slab in the tomographic models we show due to resolution. Towards Lord Howe, one model in particular, REVEAL, suggests a continuous low velocity anomaly from the region of the Vanuatu ULVZ to the surface. While the other two models do not show a continuous plume here, all models show some suggestion of hot upwelling material deflected around the South Loyalty Basin slab and down-dipping Tonga slab towards the southwest. Potentially, splitting of this plume into thinner plumelets towards the upper mantle makes it hard to image these. Alternatively, the plume may have been recently cut off by the slab and could be retreating southwards, which is consistent with an age-progressive reduction in magmatic flux observed for the Lord Howe seamount chain (Seton et al., 2019) and the lack of present-day topographic swell (Hoggard et al., 2020).

The image of two nearby broad-scale plumes, rooted by ULVZs, aligns with the 'bundle of plumes' view proposed as an explanation for LLVPs by Davaille and Romanowicz (2020). Since the connection of the ULVZ to the mantle plume and a potential hotspot is tenuous, we stick to naming it 'Vanuatu ULVZ' and not the 'Lord Howe ULVZ'. The Vanuatu and Samoa ULVZs thus represent two large scale structures at a distance of approximately 20° (~1200 km at the CMB). Future geodynamical models could test if these features can remain stable, or would be expected to eventually merge.

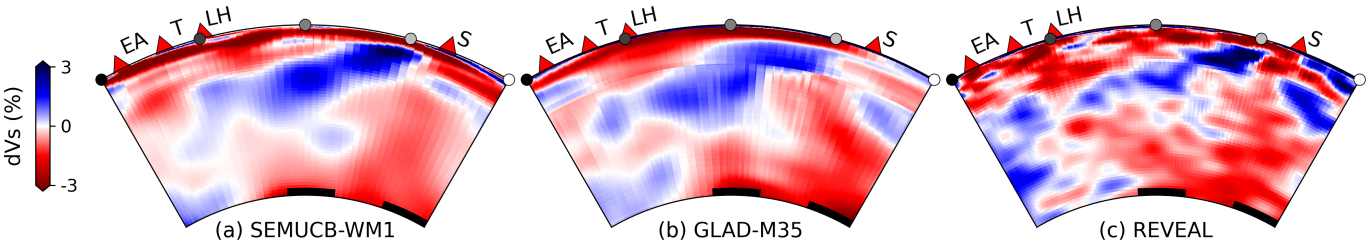

Figure 8: Cross-sections of recent whole mantle tomographic models (a) SEMUCB-WM1 (French and Romanowicz, 2014), (b) GLAD-M35 (Cui et al., 2024), and (c) REVEAL (Thrastarson et al., 2024) through the transect on Figure 3, which passes through the Vanuatu and Samoa ULVZs and near the Lord Howe and Samoa hotspots. Velocity deviations are with respect to the (whole Earth) radial average of each tomographic model. Nearby hotspots are projected onto the cross-section: EA = East Australia, T = Tasmantid, LH = Lord Howe, and S = Samoa. ULVZ thickness (solid black lines) is exaggerated for visualisation.

5 Conclusions

Sdiff+ produced by 19 earthquakes located in the South Pacific Rise region and detected by stations across East Asia provide evidence for the Vanuatu ULVZ. A combination of inverse modelling of travel times for Sdiff+ and forward modelling of Sdiff+ waveforms for six of the highest quality events places constraints on the ULVZ parameters. Since all of the earthquakes are co-located, the position of the ULVZ is well constrained in the SW-NE orientation but poorly constrained along the NW-SE direction. The preferred model of the ULVZ is a cylinder with a height of 20 ± 5 km, a radius of 240 ± 50 km, and a shear wave velocity reduction of $30 \pm 5\%$ located to the southeast of Vanuatu at $172.2 \pm 0.9°$ E and $22.9 \pm 1.1°$ S. There are strong trade-offs between the height, velocity reduction and size of the ULVZ.

Although the region surrounding the proposed location of the Vanuatu ULVZ has been intensively studied using ScP and SPdKS waveforms, our study of Sdiff+ address a gap of data coverage. Full waveform synthetics of nearby previously proposed models do not explain our observations. Joint modelling of SPdKS and Sdiff for this region may provide crucial additional constraints on the dVp/dVs ratio, and potentially density, of the ULVZ and therefore differentiate between origin hypotheses.

Synthesising our observations with previous studies suggests the CMB here is a complex landscape comprising a 'mega-ULVZ' and smaller-scale ULVZs, which is within the southwest edge of the Pacific LLVP and relatively close to the Samoa mega-ULVZ. Recent tomographic models hint at the possibility that the Vanuatu ULVZ lies at the root of a plume that is deflected to the southwest around the Tonga slab. However, tomographic models do not agree whether this plume feeds into the Lord Howe and neighbouring hotspots or if it is now a waning plume.

Acknowledgements

CM and AD were funded by a Vici award (grant number 016.160.310/526) from the Dutch Research Council (NWO). CM and SC received funding from the European Research Council (ERC) under the European Union's Horizon 2020 research and innovation programme (grant agreement No. 804071 -ZoomDeep). SC and JA received funding from the Natural Environment Research Council (NE/V018213/1 and NE/S007164/1, respectively). Some of the work in this study was performed using resources provided by the Cambridge Service for Data Driven Discovery (CSD3) operated by the University of Cambridge Research Computing Service (www.csd3.cam.ac.uk). We also acknowledge the cluster facilities, Eejit in Utrecht and Gauss in Cambridge, and thank the support staff who maintain them. We would like to thank Stuart Russell, Florian Millet, Douwe van Hinsbergen, and the Utrecht seismology group for helpful discussions; and Neil Marjoram, Lukas van de Wiel and Theo van Zessen for technical support. We thank the editor, Vernon Cormier, and two anonymous reviewers for their thoughtful comments and suggestions which improved the manuscript. Finally, we would like to thank NIED – and everyone involved with the deployment and maintenance of the seismic network infrastructure – for making such a rich data set freely available.

Data and code availability

The facilities of IRIS Data Services (www.iris.edu), and specifically the IRIS Data Management Center, were used for access to waveforms and related metadata. IRIS Data Services are funded through the Seismological Facilities for the Advancement of Geoscience (SAGE) Award of the National Science Foundation under Cooperative Support Agreement EAR-1851048. Data from the F-net and Hi-net networks were made freely available by National Research Institute for Earth Science and Disaster Resilience (Okada et al., 2004). Data from NIED was downloaded using HinetPy (Tian, 2024). Earthquake parameters were used from the Global CMT Project (www.globalcmt.org). Codes used will be made available by CM upon request.

Competing interests

Authors declare that they have no competing interests.

References

Bodin, T. and M. Sambridge (2009). Seismic tomography with the reversible jump algorithm. *Geophys. J. Int.* 178.3, 1411–1436. DOI: 10.1111/j.1365-246X.2009.04226.x.

Bower, D. J., J. K. Wicks, M. Gurnis, and J. M. Jackson (2011). A geodynamic and mineral physics model of a solid-state ultralow-velocity zone. *Earth Planet. Sci. Lett.* 303.3-4, 193–202. DOI: 10.1016/j.epsl.2010.12.035.

Brown, S. P., M. S. Thorne, L. Miyagi, and S. Rost (2015). A compositional origin to ultralow-velocity zones. *Geophys. Res. Lett.* 42.4, 1039–1045. DOI: 10.1002/2014GL062097.

Cottaar, S. and V. Lekic (2016). Morphology of seismically slow lower-mantle structures. *Geophys. J. Int.* 207.2, 1122–1136. DOI: 10.1093/gji/ggw324.

Cottaar, S., C. Martin, Z. Li, and R. Parai (2022). The root to the Galápagos mantle plume on the core-mantle boundary. *Seismica* 1.1. DOI: 10.26443/seismica.v1i1.197.

Cottaar, S. and B. Romanowicz (2012). An unusally large ULVZ at the base of the mantle near Hawaii. *Earth Planet. Sci. Lett.* 355, 213–222. DOI: 10.1016/j.epsl.2012.09.005.

Crotwell, H. P., T. J. Owens, J. Ritsema, et al. (1999). The TauP Toolkit: Flexible seismic travel-time and ray-path utilities. *Seismol. Res. Lett.* 70, 154–160. DOI: 10.1785/gssrl.70.2.154.

Cui, C., W. Lei, Q. Liu, D. Peter, E. Bozdağ, J. Tromp, J. Hill, N. Podhorszki, and D. Pugmire (2024). GLAD-M35: a joint P and S global tomographic model with uncertainty quantification. *Geophys. J. Int.* 239.1, 478–502. DOI: 10.1093/gji/ggae270.

Dannberg, J., R. Myhill, R. Gassmöller, and S. Cottaar (2021). The morphology, evolution and seismic visibility of partial melt at the core–mantle boundary: implications for ULVZs. *Geophys. J. Int.* 227.2, 1028–1059. DOI: 10.1093/gji/ggab242.

Davaille, A. and B. Romanowicz (2020). Deflating the LLSVPs: Bundles of mantle thermochemical plumes rather than thick stagnant "piles". *Tectonics* 39.10, e2020TC006265. DOI: 10.1029/2020TC006265.

Davison, S., C. Martin, R. Parai, and S. Cottaar (2024). Ultra-low velocity zone beneath the Atlantic near St. Helena. *Geochem. Geophys. Geosyst.* 25.7, e2024GC011559. DOI: 10.1029/2024GC011559.

Dobrosavljevic, V. V., W. Sturhahn, and J. M. Jackson (2019). Evaluating the role of iron-rich (Mg, Fe) O in ultralow velocity zones. *Minerals* 9.12, 762. DOI: 10.3390/min9120762.

Driel, M. van, L. Krischer, S. C. Stähler, K. Hosseini, and T. Nissen-Meyer (2015). Instaseis: instant global seismograms based on a broadband waveform database. *Solid Earth* 6.2, 701–717. DOI: 10.5194/se-6-701-2015.

Dziewonski, A. M. and D. L. Anderson (1981). Preliminary reference Earth model. *Phys. Earth Planet. Inter.* 25.4, 297–356. DOI: 10.1016/0031-9201(81)90046-7.

Ekström, G., M. Nettles, and A. M. Dziewonski (2012). The global CMT project 2004-2010: Centroid-moment tensors for 13,017 earthquakes. *Phys. Earth Planet. Inter.* 200-201, 1–9. DOI: 10.1016/j.pepi.2012.04.002.

Esdaille, S. S. and J. Chen (2024). Mineral physics constraints on ultra-low velocity zones in the lowermost mantle. *Earth-Sci. Rev.* 250, 104685. DOI: 10.1016/j.earscirev.2024.104685.

Festin, M. M., M. S. Thorne, and M. Li (2024). Evidence for ultra-low velocity zone genesis in downwelling subducted slabs at the core–mantle boundary. *Seism. Rec.* 4.2, 111–120. DOI: 10.1785/0320240003.

French, S. and B. A. Romanowicz (2014). Whole-mantle radially anisotropic shear velocity structure from spectral-element waveform tomography. *Geophys. J. Int.* 199.3, 1303–1327. DOI: 10.1093/gji/ggu334.

Fu, S., S. Chariton, V. B. Prakapenka, and S.-H. Shim (2023). Core origin of seismic velocity anomalies at Earth's core–mantle boundary. *Nature* 615.7953, 646–651. DOI: 10.1038/s41586-023-05713-5.

Garnero, E. J., A. K. McNamara, and S.-H. Shim (2016). Continent-sized anomalous zones with low seismic velocity at the base of Earth's mantle. *Nat. Geo.* 9.7, 481–489. DOI: 10.1038/ngeo2733.

Hansen, S. E., S. E. Carson, E. J. Garnero, S. Rost, and S. Yu (2020). Investigating ultra-low velocity zones in the southern hemisphere using an Antarctic dataset. *Earth Planet. Sci. Lett.* 536, 116142. DOI: 10.1016/j.epsl.2020.116142.

Hansen, S. E., E. J. Garnero, M. Li, S.-H. Shim, and S. Rost (2023). Globally distributed subducted materials along the Earth's core-mantle boundary: Implications for ultralow velocity zones. *Sci. Adv.* 9.14, eadd4838. DOI: 10.1126/sciadv.add4838.

Hauser, J., M. Sambridge, and N. Rawlinson (2008). Multi-arrival wavefront tracking and its applications. *Geochem. Geophys. Geosyst.* 9.11. DOI: 10.1029/2008GC002069.

Hernlund, J. W. and A. M. Jellinek (2010). Dynamics and structure of a stirred partially molten ultralow-velocity zone. *Earth Planet. Sci. Lett.* 296.1-2, 1–8. DOI: 10.1016/j.epsl.2010.04.027.

Hernlund, J. W. and P. J. Tackley (2007). Some dynamical consequences of partial melting in Earth's deep mantle. *Phys. Earth Planet. Inter.* 162.1-2, 149–163. DOI: 10.1016/j.pepi.2007.04.005.

Herret, M.-T., B. J. Peters, D. Kim, P. Castillo, and A. Mundl-Petermeier (2023). Decoupling of short-lived radiogenic and helium isotopes in the Marquesas hotspot. *Chem. Geol.* 640, 121727. DOI: 10.1016/j.chemgeo.2023.121727.

Hoggard, M. J., R. Parnell-Turner, and N. White (2020). Hotspots and mantle plumes revisited: Towards reconciling the mantle heat transfer discrepancy. *Earth Planet. Sci. Lett.* 542, 116317. DOI: 10.1016/j.epsl.2020.116317.

Idehara, K., A. Yamada, and D. Zhao (2007). Seismological constraints on the ultralow velocity zones in the lowermost mantle from core-reflected waves. *Phys. Earth Planet. Inter.* 165.1-2, 25–46. DOI: 10.1016/j.pepi.2007.07.005.

Jellinek, A. M. and M. Manga (2002). The influence of a chemical boundary layer on the fixity, spacing and lifetime of mantle plumes. *Nature* 418.6899, 760–763. DOI: 10.1038/nature00979.

Jenkins, J., S. Mousavi, Z. Li, and S. Cottaar (2021). A high-resolution map of Hawaiian ULVZ morphology from ScS phases. *Earth Planet. Sci. Lett.* 563, 116885. DOI: 10.1016/j.epsl.2021.116885.

Jensen, K. J., M. S. Thorne, and S. Rost (2013). SPdKS analysis of ultralow-velocity zones beneath the western Pacific. *Geophys. Res. Lett.* 40.17, 4574–4578. DOI: 10.1002/grl.50877.

Kim, D., V. Lekić, B. Ménard, D. Baron, and M. Taghizadeh-Popp (2020). Sequencing seismograms: A panoptic view of scattering in the core-mantle boundary region. *Science* 368.6496, 1223–1228. DOI: 10.1126/science.aba8972.

Koelemeijer, P., A. Deuss, and J. Ritsema (2017). Density structure of Earth's lowermost mantle from Stoneley mode splitting observations. *Nat. Commun.* 8.1, 15241. DOI: 10.1038/ncomms15241.

Koelemeijer, P., A. Deuss, and J. Trampert (2012). Normal mode sensitivity to Earth's D"' layer and topography on the core-mantle boundary: what we can and cannot see. *Geophys. J. Int.* 190.1, 553–568. DOI: 10.1111/j.1365-246X.2012.05499.x.

Komatitsch, D., L. P. Vinnik, and S. Chevrot (2010). SHdiff-SVdiff splitting in an isotropic Earth. *J. Geophys. Res., Solid Earth* 115.B7. DOI: 10.1029/2009JB006795.

Krier, J., M. S. Thorne, K. Leng, and T. Nissen-Meyer (2021). A compositional component to the Samoa ultralow-velocity zone revealed through 2-and 3-D waveform modeling of SKS and SKKS differential travel-times and amplitudes. *J. Geophys. Res., Solid Earth* 126.7, e2021JB021897. DOI: 10.1029/2021JB021897.

Labrosse, S., J. Hernlund, and N. Coltice (2007). A crystallizing dense magma ocean at the base of the Earth's mantle. *Nature* 450.7171, 866–869. DOI: 10.1038/nature06355.

Lau, H. C., J. X. Mitrovica, J. L. Davis, J. Tromp, H.-Y. Yang, and D. Al-Attar (2017). Tidal tomography constrains Earth's deep-mantle buoyancy. *Nature* 551.7680, 321–326. DOI: 10.1038/nature24452.

Leng, K., T. Nissen-Meyer, M. Van Driel, K. Hosseini, and D. Al-Attar (2019). AxiSEM3D: broad-band seismic wavefields in 3-D global Earth models with undulating discontinuities. *Geophys. J. Int.* 217.3, 2125–2146. DOI: 10.1093/gji/ggz092.

Li, J., D. Sun, and D. J. Bower (2022). Slab control on the megasized North Pacific ultra-low velocity zone. *Nat. Commun.* 13.1, 1042. DOI: 10.1038/s41467-022-28708-8.

Li, M. (2023). Variable distribution of subducted oceanic crust beneath subduction regions of the lowermost mantle. *Phys. Earth Planet. Inter.* 341, 107063. DOI: 10.1016/j.pepi.2023.107063.

Li, Z., K. Leng, J. Jenkins, and S. Cottaar (2022). Kilometer-scale structure on the core–mantle boundary near Hawaii. *Nat. Commun.* 13.1, 2787. DOI: 10.1038/s41467-022-30502-5.

Li, Z., C. Martin, and S. Cottaar (2024). Seismic observation of a new ULVZ beneath the Southern Pacific. *J. Geophys. Res., Solid Earth* 129.4, e2023JB026941. DOI: 10.1029/2023JB026941.

Liu, X., F. Tian, J. Li, Y. Li, and W. Sun (2024). The evolution of dense ULVZs originating outside LLSVPs and implications for dynamics at LLSVP margins. *J. Geophys. Res., Solid Earth* 129.12, e2024JB028972. DOI: 10.1029/2024JB028972.

Martin, C., T. Bodin, and S. Cottaar (2023a). Mapping structures on the core–mantle boundary using Sdiff postcursors: Part I. Method and Validation. *Geophys. J. Int.* 235.3, 2385–2398. DOI: 10.1093/gji/ggad340.

Martin, C., T. Bodin, and S. Cottaar (2023b). Mapping structures on the core–mantle boundary using Sdiff postcursors: Part II. Application to the Hawaiian ULVZ. *Geophys. J. Int.* 235.3, 2399–2409. DOI: 10.1093/gji/ggad345.

Martin, C., S. Russell, and S. Cottaar (2024). Detection of a ULVZ in the Central Pacific using high frequency Sdiff postcursors. *Earth Planet. Sci. Lett.* 648, 119028. DOI: 10.1016/j.epsl.2024.119028.

Mundl-Petermeier, A., R. Walker, R. Fischer, V. Lekic, M. Jackson, and M. Kurz (2020). Anomalous ^{1}82W in high ^{3}He/^{4}He ocean island basalts: Fingerprints of Earth's core? *Geochim. Cosmochim. Acta* 271, 194–211. DOI: 10.1016/j.gca.2019.12.020.

Okada, Y., K. Kasahara, S. Hori, K. Obara, S. Sekiguchi, H. Fujiwara, and A. Yamamoto (2004). Recent progress of seismic observation networks in Japan—Hi-net, F-net, K-NET and KiK-net. *Earth Planets Space* 56, xv–xxviii. DOI: 10.1186/BF03353076.

Pachhai, S., J. Dettmer, and H. Tkalčić (2015). Ultra-low velocity zones beneath the Philippine and Tasman Seas revealed by a trans-dimensional Bayesian waveform inversion. *Geophys. J. Int.* 203.2, 1302–1318. DOI: 10.1093/gji/ggv368.

Pachhai, S., M. Li, M. S. Thorne, J. Dettmer, and H. Tkalčić (2022). Internal structure of ultralow-velocity zones consistent with origin from a basal magma ocean. *Nat. Geo.* 15.1, 79–84. DOI: 10.1038/s41561-021-00871-5.

Pachhai, S., M. S. Thorne, and S. Rost (2023). Improved characterization of ultralow-velocity zones through advances in Bayesian inversion of ScP waveforms. *J. Geophys. Res., Solid Earth* 128.6, e2023JB026415. DOI: 10.1029/2023JB026415.

Pachhai, S., M. S. Thorne, and S. Rost (2024). Examining the influence of 2.5-D ultra-low velocity zone morphology on ScP waveforms and estimated elastic parameters. *Geophys. J. Int.* 239.1, 591–620. DOI: 10.1093/gji/ggae285.

Richards, F. D., M. J. Hoggard, S. Ghelichkhan, P. Koelemeijer, and H. C. Lau (2023). Geodynamic, geodetic, and seismic constraints favour deflated and dense-cored LLVPs. *Earth Planet. Sci. Lett.* 602, 117964. DOI: 10.1016/j.epsl.2022.117964.

Ritsema, J., A. Deuss, H. Van Heijst, and J. Woodhouse (2011). S40RTS: a degree-40 shear-velocity model for the mantle from new Rayleigh wave dispersion, teleseismic traveltime and normal-mode splitting function measurements. *Geophys. J. Int.* 184.3, 1223–1236. DOI: 10.1111/j.1365-246X.2010.04884.x.

Rogers, A., M. Flanigan, O. Nebel, Y. Nebel-Jacobsen, X. Wang, R. J. Arculus, L. Miller, I. Smith, B. R. Mather, M. Kendrick, et al. (2023). The isotopic origin of Lord Howe Island reveals secondary mantle plume twinning in the Tasman Sea. *Chem. Geol.* 622, 121374. DOI: 10.1016/j.chemgeo.2023.121374.

Rost, S., E. J. Garnero, and W. Stefan (2010). Thin and intermittent ultralow-velocity zones. *J. Geophys. Res., Solid Earth* 115.B6. DOI: 10.1029/2009JB006981.

Rost, S., E. J. Garnero, and Q. Williams (2006). Fine-scale ultralow-velocity zone structure from high-frequency seismic array data. *J. Geophys. Res., Solid Earth* 111.B9. DOI: 10.1029/2005JB004088.

Rost, S., E. J. Garnero, Q. Williams, and M. Manga (2005). Seismological constraints on a possible plume root at the core–mantle boundary. *Nature* 435.7042, 666–669. DOI: 10.1038/nature03620.

Rost, S. and J. Revenaugh (2001). Seismic detection of rigid zones at the top of the core. *Science* 294.5548, 1911–1914. DOI: 10.1126/science.1065617.

Rost, S. and J. Revenaugh (2003). Small-scale ultralow-velocity zone structure imaged by ScP. *J. Geophys. Res., Solid Earth* 108.B1. DOI: 10.1029/2001JB001627.

Russell, S., J. C. Irving, and S. Cottaar (2022). Seismic visibility of melt at the core-mantle boundary from PKKP diffracted waves. *Earth Planet. Sci. Lett.* 595, 117768. DOI: 10.1016/j.epsl.2022.117768.

Russell, S., J. C. Irving, L. Jagt, and S. Cottaar (2023). Evidence for a kilometer-scale seismically slow layer atop the core-mantle boundary from normal modes. *Geophys. Res. Lett.* 50.24, e2023GL105684. DOI: 10.1029/2023GL105684.

Russell, S., J. K. Magali, K. Vallenton, and C. Thomas (2025). The effect of source-side subduction on PKP differential times and implications for inner core anisotropy. *Phys. Earth Planet. Inter.*, 107382. DOI: 10.1016/j.pepi.2025.107382.

Schellart, W. P., B. Kennett, W. Spakman, and M. Amaru (2009). Plate reconstructions and tomography reveal a fossil lower mantle slab below the Tasman Sea. *Earth Planet. Sci. Lett.* 278.3-4, 143–151. DOI: 10.1016/j.epsl.2008.11.004.

Seton, M., S. Williams, N. Mortimer, S. Meffre, S. Micklethwaite, and S. Zahirovic (2019). Magma production along the Lord Howe seamount chain, northern Zealandia. *Geol. Mag.* 156.9, 1605–1617. DOI: 10.1017/S0016756818000912.

Talavera-Soza, S., L. Cobden, U. H. Faul, and A. Deuss (2025). Global 3D model of mantle attenuation using seismic normal modes. *Nature*, 1–5. DOI: 10.1038/s41586-024-08322-y.

Thomas, C., J.-M. Kendall, and G. Helffrich (2009). Probing two low-velocity regions with PKP b-caustic amplitudes and scattering. *Geophys. J. Int.* 178.1, 503–512. DOI: 10.1111/j.1365-246X.2009.04189.x.

Thomas, C., M. Weber, C. Wicks, and F. Scherbaum (1999). Small scatterers in the lower mantle observed at German broadband arrays. *J. Geophys. Res., Solid Earth* 104.B7, 15073–15088. DOI: 10.1029/1999JB900128.

Thorne, M. S. and E. J. Garnero (2004). Inferences on ultralow-velocity zone structure from a global analysis of SPdKS waves. *J. Geophys. Res., Solid Earth* 109.B8. DOI: 10.1029/2004JB003010.

Thorne, M. S., E. J. Garnero, G. Jahnke, H. Igel, and A. K. McNamara (2013). Mega ultra low velocity zone and mantle flow. *Earth Planet. Sci. Lett.* 364, 59–67. DOI: 10.1016/j.epsl.2012.12.034.

Thorne, M. S., K. Leng, S. Pachhai, S. Rost, J. Wicks, and T. Nissen-Meyer (2021). The most parsimonious ultralow-velocity zone distribution from highly anomalous SPdKS waveforms. *Geochem. Geophys. Geosyst.* 22.1, e2020GC009467. DOI: 10.1029/2020GC009467.

Thrastarson, S., D.-P. van Herwaarden, S. Noe, C. Josef Schiller, and A. Fichtner (2024). REVEAL: A global full-waveform inversion model. *Bull. Seismol. Soc. Am.* 114.3, 1392–1406. DOI: 10.1785/0120230273.

Tian, D. (2024). HinetPy: A Python package for accessing and processing NIED Hi-net seismic data. *J. Open Source Softw.* 9.98, 6840. DOI: 10.21105/joss.06840.

Van der Meer, D. G., D. J. Van Hinsbergen, and W. Spakman (2018). Atlas of the underworld: Slab remnants in the mantle, their sinking history, and a new outlook on lower mantle viscosity. *Tectonophysics* 723, 309–448. DOI: 10.1016/j.tecto.2017.10.004.

Wicks, J., J. Jackson, and W. Sturhahn (2010). Very low sound velocities in iron-rich (Mg, Fe) O: Implications for the core-mantle boundary region. *Geophys. Res. Lett.* 37.15. DOI: 10.1029/2010GL043689.

Williams, Q., J. Revenaugh, and E. Garnero (1998). A correlation between ultra-low basal velocities in the mantle and hot spots. *Science* 281.5376, 546–549. DOI: 10.1126/science.281.5376.546.

Wolf, J. and M. D. Long (2023). Lowermost mantle structure beneath the central Pacific Ocean: Ultralow velocity zones and seismic anisotropy. *Geochem. Geophys. Geosyst.* 24.6, e2022GC010853. DOI: 10.1029/2022GC010853.

Yu, S. and E. J. Garnero (2018). Ultralow velocity zone locations: a global assessment. *Geochem. Geophys. Geosyst.* 19.2, 396–414. DOI: 10.1002/2017GC007281.

Yuan, K. and B. Romanowicz (2017). Seismic evidence for partial melting at the root of major hot spot plumes. *Science* 357.6349, 393–397. DOI: 10.1126/science.aan0760.

Evidence of a ULVZ near Vanuatu from Sdiff postcursors

Carl Martin[1*], Lobke Harmsma[1], James Atkins[2], Arwen Deuss[1], Sanne Cottaar[2]

[1] Department of Geosciences, Utrecht University, 3584 CB, Netherlands

[2] Bullard Laboratories, Department of Earth Sciences, University of Cambridge, CB3 0EZ, UK

*Corresponding author (c.d.martin@uu.nl)

SUPPLEMENTARY

In this supplementary are:

- Section S1: Earthquake data used in this study
- Section S2: Waveforms of synthetics for different parameters to demonstrate trade-offs
- Section S3: Waveform modelling of ULVZs in earlier studies for comparison

S1 Earthquake data

S1.1 Earthquake list

In total we identified 19 earthquakes in the South Pacific Rise region towards seismic arrays East Asia – particularly the Japanese F-net [Okada et al., 2004] – which showed Sdiff postcursor evidence of a ULVZ (Table S1).

	Date	**Lon.** [°E]	**Lat.** [°N]	Depth [km]	**Mag.**	**Location**
	2001/08/06	-123.05	-55.67	15	Mw 6.7	Southern East Pacific Rise
3	2001/09/02	-136.75	-54.31	15	Mw 6.3	Pacific-Antarctic Ridge
1	2003/08/28	-115.20	-49.92	15	Mw 6.2	Southern East Pacific Rise
	2004/01/29	-114.85	-50.03	15	Mw 6.1	Southern East Pacific Rise
2	2005/05/12	-138.91	-57.57	12	Mw 6.5	Pacific-Antarctic Ridge
	2006/10/10	-122.41	-56.18	12	Mw 6.0	Southern East Pacific Rise
4a	2007/03/31	-123.61	-55.94	12	Mw 6.2	Southern East Pacific Rise
	2007/11/02	-128.80	-55.40	13.55	Mw 6.2	Pacific-Antarctic Ridge
	2011/11/02	-129.08	-55.34	15	Mw 6.2	Pacific-Antarctic Ridge
	2012/07/18	-128.96	-55.36	20.34	Mw 5.9	Pacific-Antarctic Ridge
	2014/05/12	-115.06	-49.90	13.24	Mw 6.4	Southern East Pacific Rise
5	2015/05/19	-132.39	-54.53	14.91	Mw 6.6	Pacific-Antarctic Ridge
	2015/12/24	-123.11	-56.06	12.13	Mww 6.2	Southern East Pacific Rise
	2016/02/16	-124.57	-55.74	20.13	Mww 6.1	Southern East Pacific Rise
4b	2016/08/18	-123.63	-55.97	13.44	Mw 6.0	Southern East Pacific Rise
	2017/06/15	-124.44	-55.77	20.03	Mww 5.8	Southern East Pacific Rise
	2018/11/15	-122.26	-56.23	12	Mww 6.3	Southern East Pacific Rise
	2024/05/18	-123.14	-56.05	12	Mww 5.9	Southern East Pacific Rise
	2024/06/09	-133.88	-54.06	12.62	Mww 6.2	Pacific-Antarctic Ridge

Table S1. Earthquake data and parameters for events showing Sdiff postcursors that sample the CMB near Vanuatu. This study uses the events labelled 1–5 (Table 1 in main paper). Event locations are plotted in Figure 3. Earthquake parameters and moment tensor solutions are taken from the Global CMT Project [Ekström et al., 2012].

S1.2 Events used in the study

We reproduce Figure 4, showing the waveforms for six earthquakes, Events 1–5, filtered between 7–12, 20–30 and 30–40 s period (Figures S1–S3, respectively). We also plot displacement waveforms from the Hi-net short period seismometers filtered between 10–20 and 7–12 s period (Figures S4 & S5, respectively) [Okada et al., 2004].

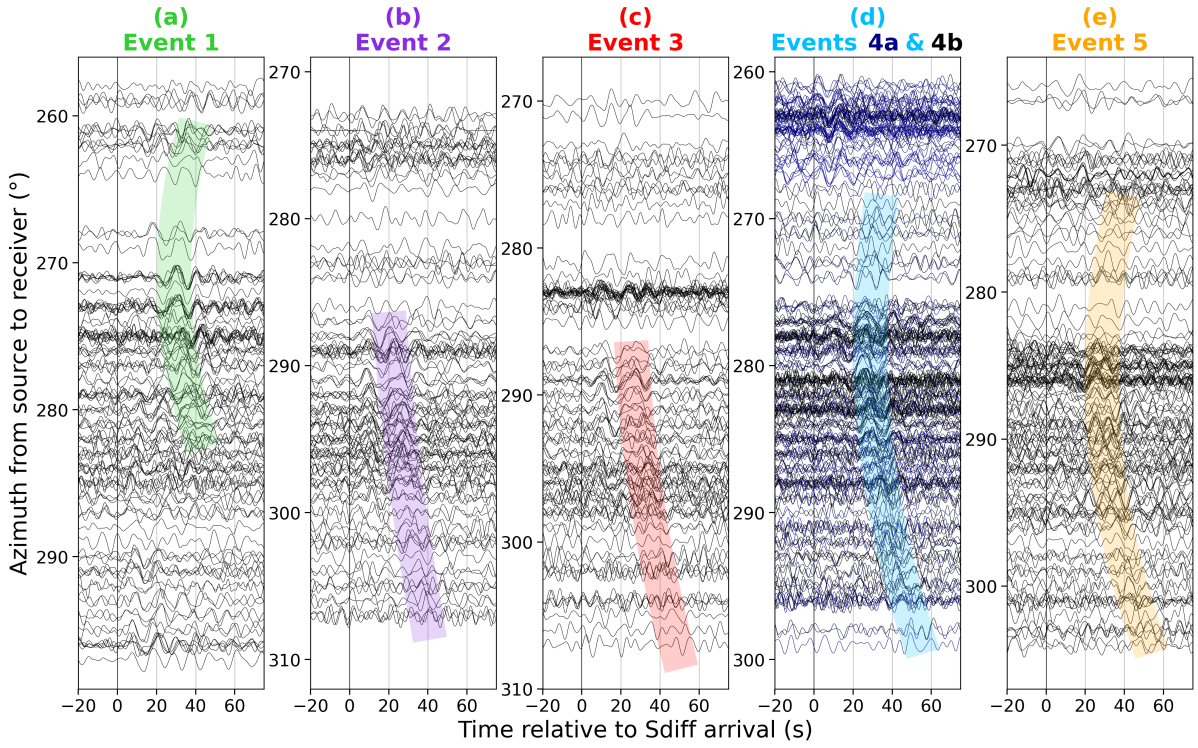

Figure S1. Same as Figure 4 but filtered between 7–12 s period.

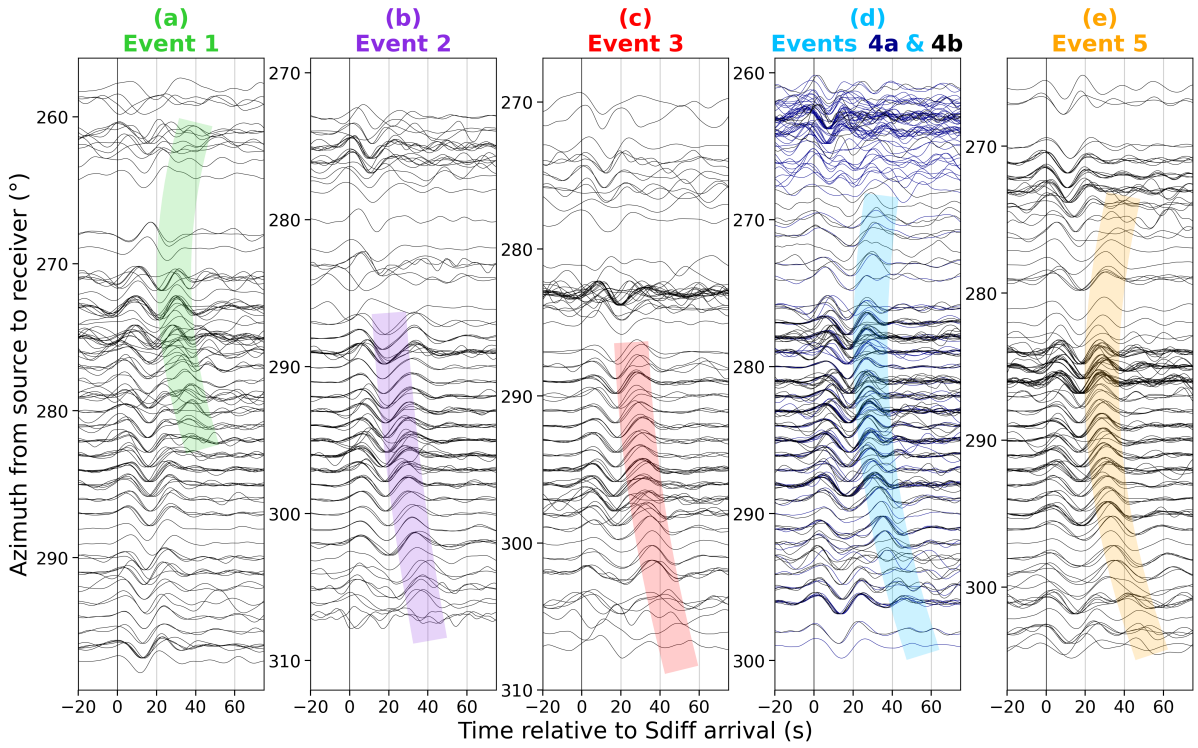

Figure S2. Same as Figure 4 but filtered between 20–30 s period.

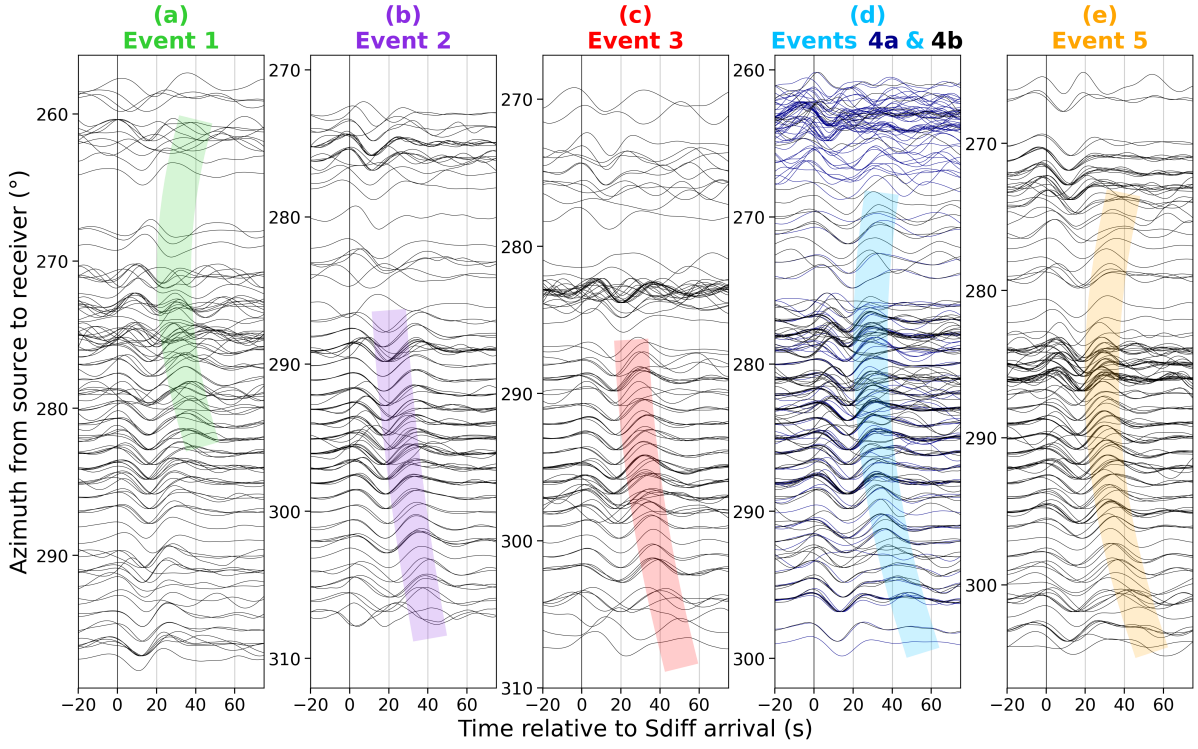

Figure S3. Same as Figure 4 but filtered between 30–40 s period.

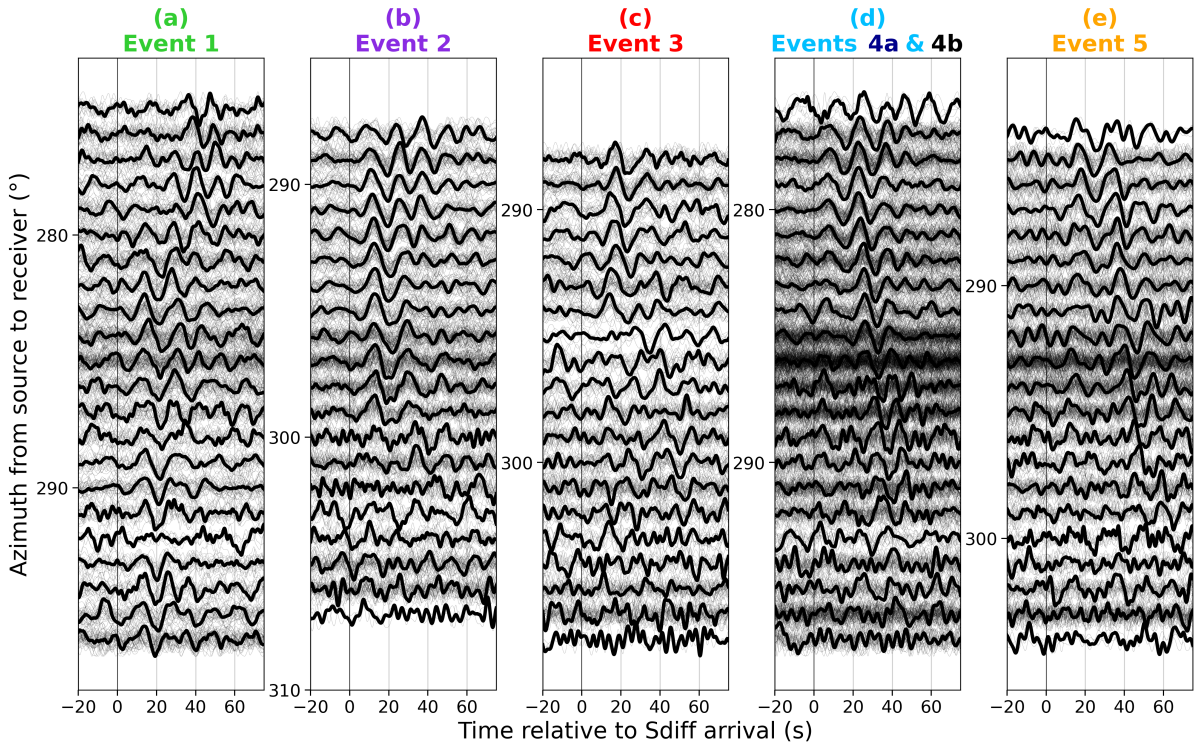

Figure S4. Displacement waveforms from the short period Hi-net seismometers for Events 1–5 filtered between 10–20 s period. The linear stack of each 1° azimuthal bin (thick black lines) overlay the individual seismograms (thin grey lines). Note the different (y axis) azimuthal range compared to broadband data.

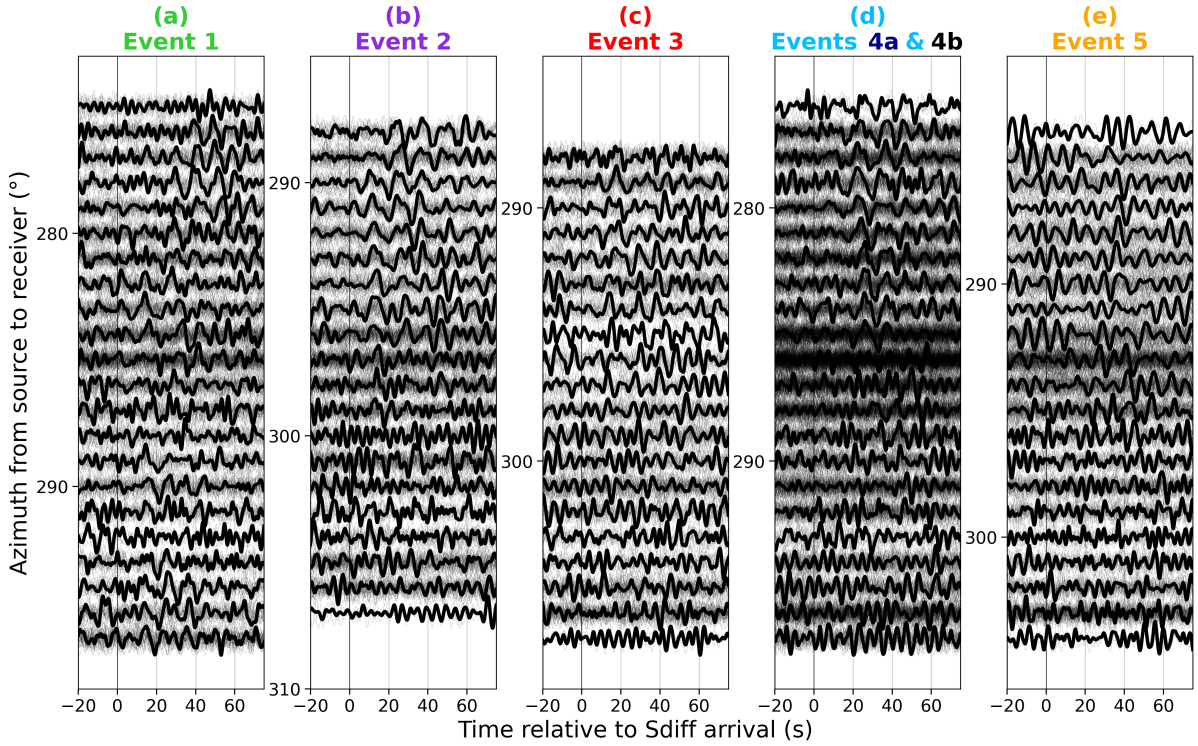

Figure S5. Same as Figure S4 but filtered between 7–12 s period.

S2 Trade-offs in waveform modelling

Figure S6 shows the synthetics predicted for the source solutions from the Global CMT Project with the depth set to 0 km which best matches the observed Sdiff waveforms. We note that the data and synthetics for Event 2 have been flipped to match the waveforms of the other events for ease of visual comparison.

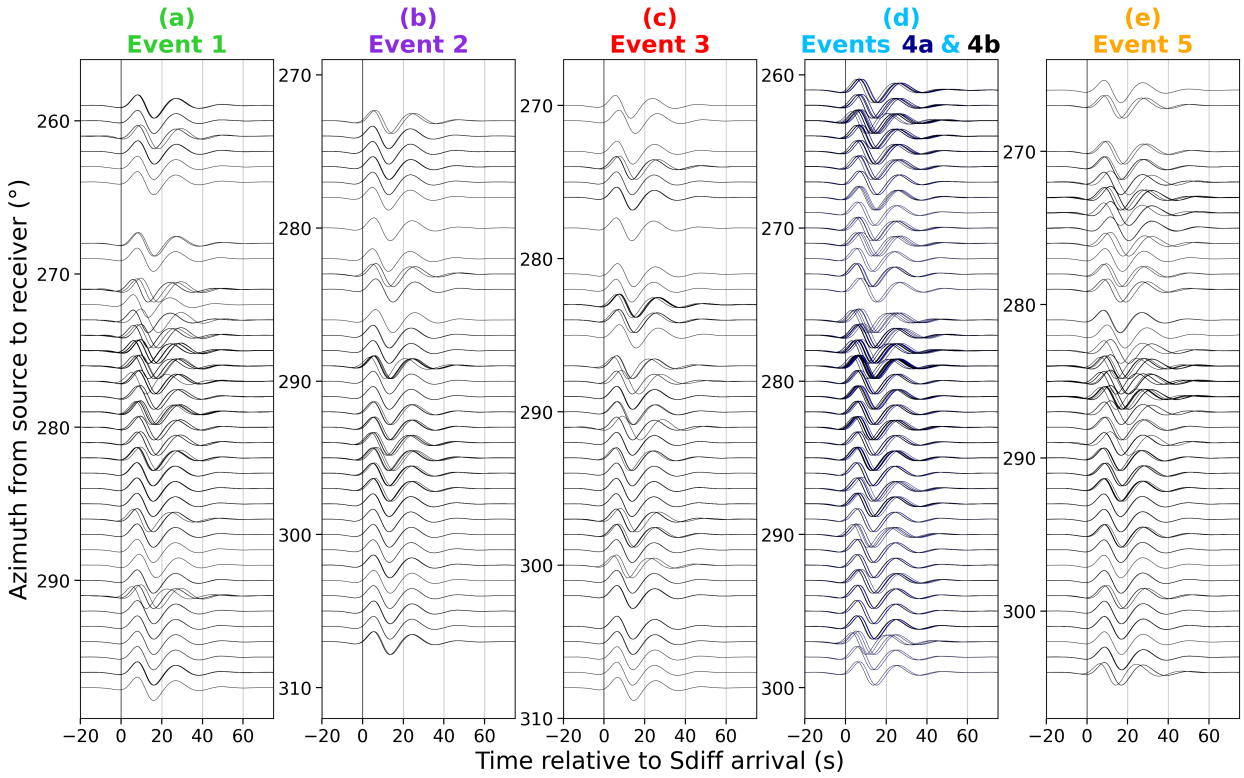

Figure S6. Displacement synthetics for PREM filtered between periods of 10–20 s for the six events listed in Table 1. Earthquake parameters and moment tensor solutions are taken from the Global CMT Project [Ekström et al., 2012], with depths set to 0 km.

We explore the trade-off in model parameters now using full waveform synthetics. The location and uncertainties are inferred from the 2DWT inversion (Figure 5a), which are assumed to be fixed for the remainder of this uncertainty assessment. We trial a number of models along the velocity-size trade-off curve of the 2DWT ensemble to demonstrate that this trade-off is reproduced by full waveform synthetics as well as some off-curve parameters (Figure S7 & Table S2). Additionally, we constrain the height by comparing the presence or absence of postcursors in synthetics with ULVZs of heights 15, 20, 25 and 30 km for different filter bands. We also show predicted travel times from the 2DWT for the various models listed in Table S2 (Figure S8).

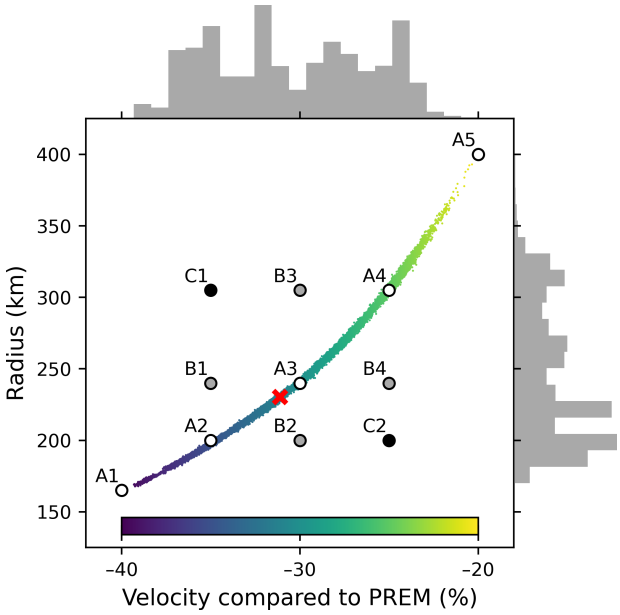

Figure S7. Duplicate of Figure 5b, with parameter labels overlaid. Ensemble of models that fit the Sdiff postcursor arrival times, showing the trade-off in velocity and size. The median model is marked with a red cross and histograms of each of the parameters are projected onto the respective axes.

Model	dVs (%)	R (km)	H (km)
A1	−40	165	20
A2	−35	200	20
A3	−30	240	20+15,25,30
A4	−25	305	20
A5	−20	400	20
B1	−35	240	20
B2	−30	200	20
B3	−30	305	20
B4	−25	240	20
C1	−35	305	20
C2	−25	200	20

Table S2. Parameters used to test 3D cylindrical models of the ULVZ. All models are centred at the median location, 172.16 °E and 22.92 °S. Synthetics are also run for Model A3 with heights 15, 25, and 30 km to demonstrate sensitivity of the frequency content of the waveforms to model height.

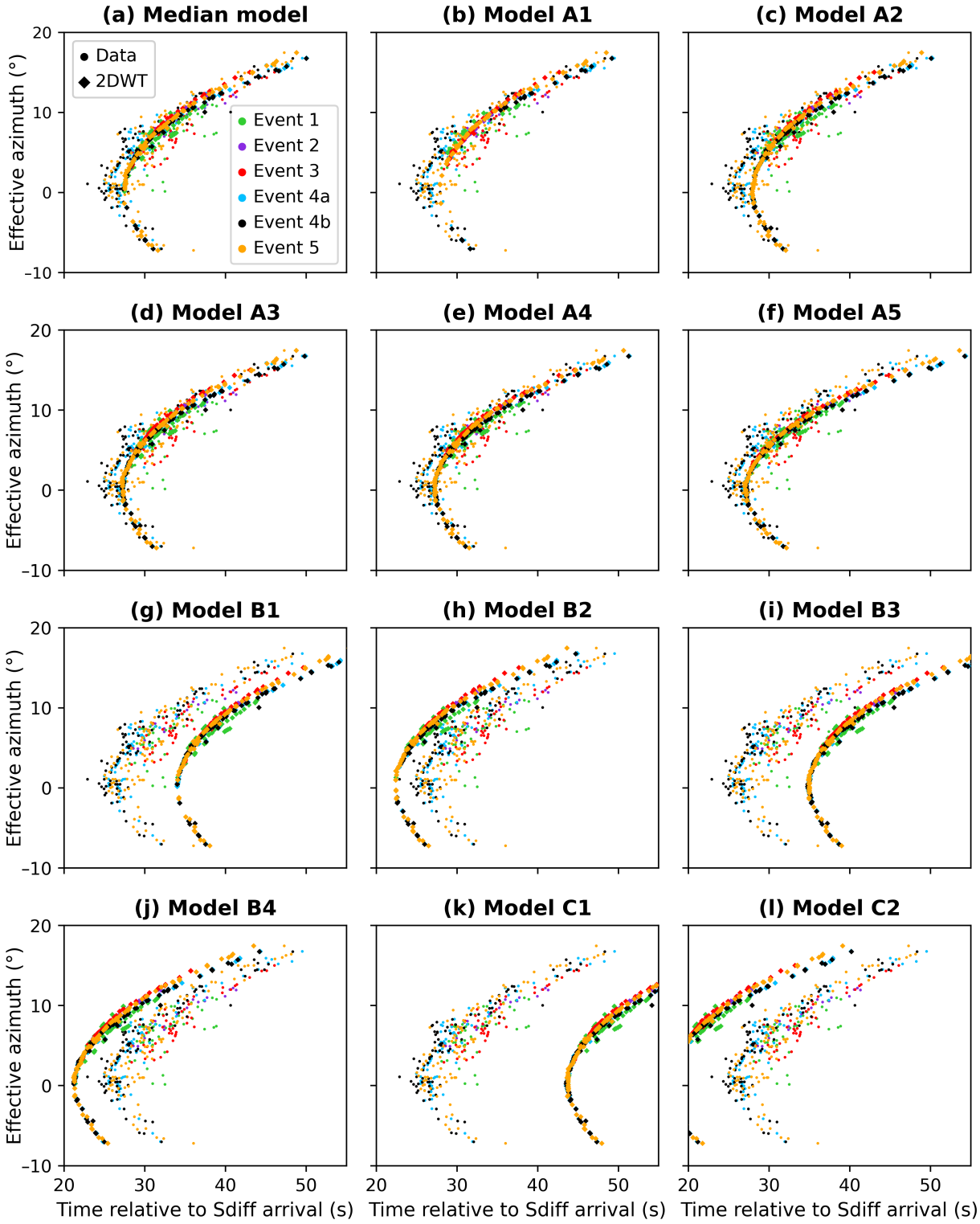

Figure S8. Predicted travel times from the 2DWT for the various models for which we compute full waveform synthetics (Figure S7 & Table S2). (a) is the same as Figure 5c. Note that the 2DWT predictions do not account for height of the model.

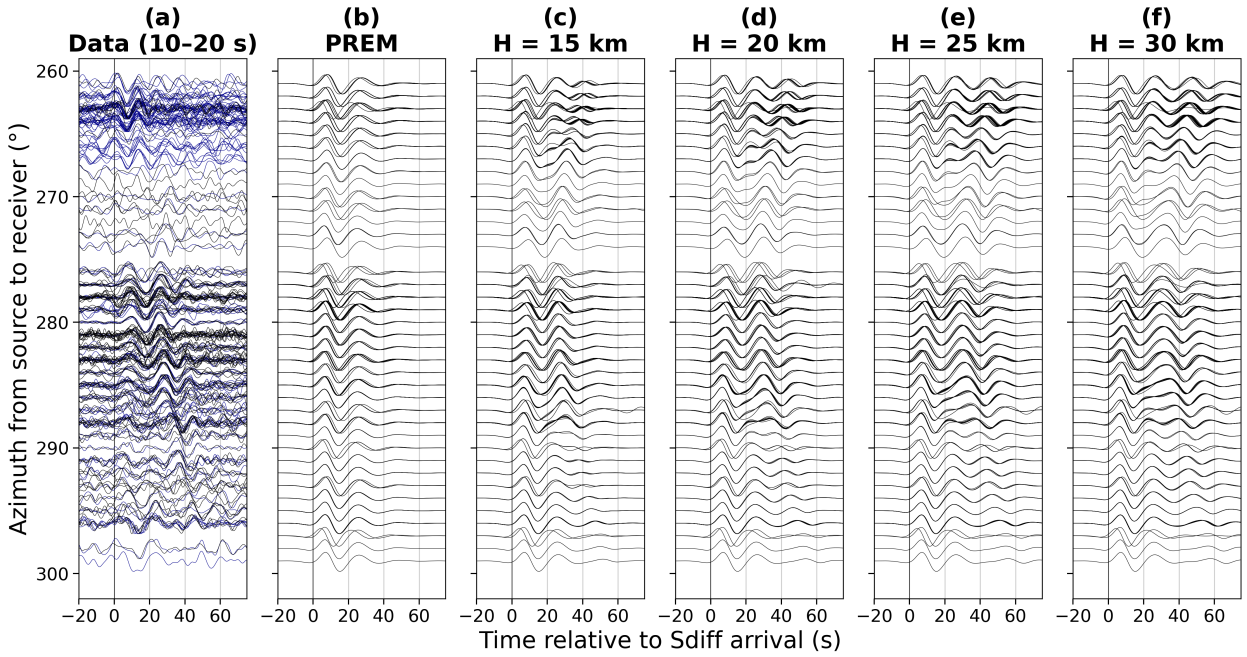

Figure S9. (a) Real data and synthetic waveforms for (b) PREM with no ULVZ and PREM with a cylindrical ULVZ of height (c) 15 km, (d) 20 km, (e) 25 km, and (f) 30 km for Events 4a & 4b, filtered between 10–20 s period. All models use dVs of -30% and a radius of 240 km (Model A3, Table S2).

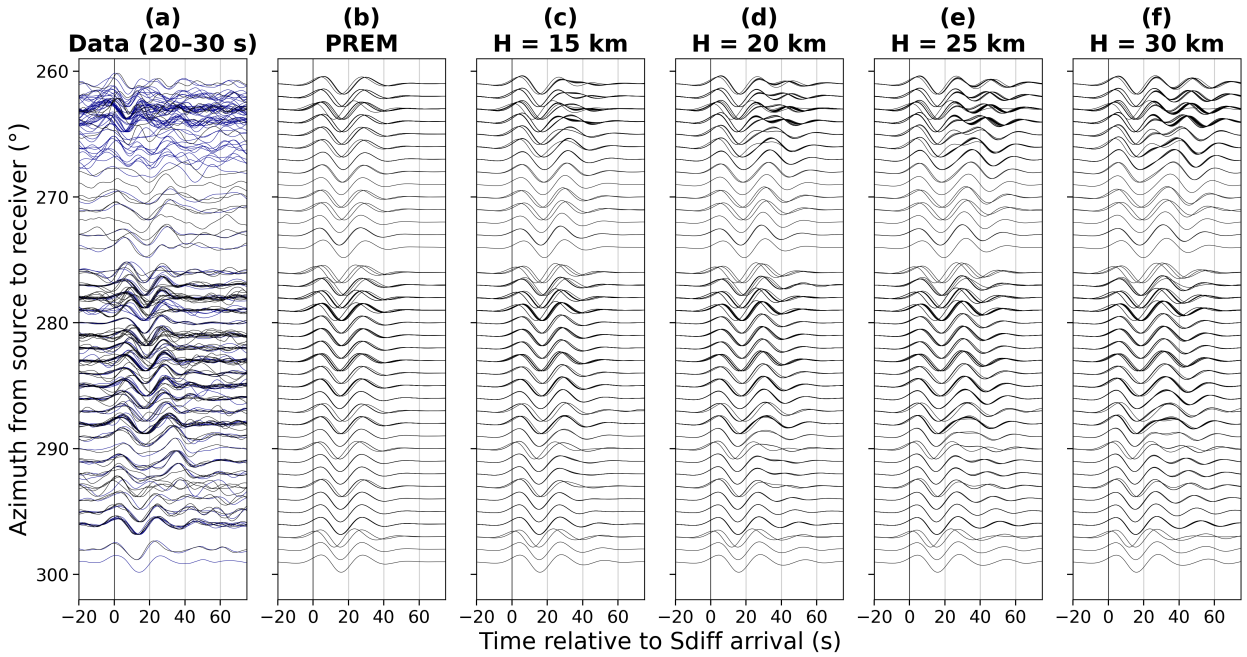

Figure S10. Same as Figure S9 but filtered between 20–30 s period.

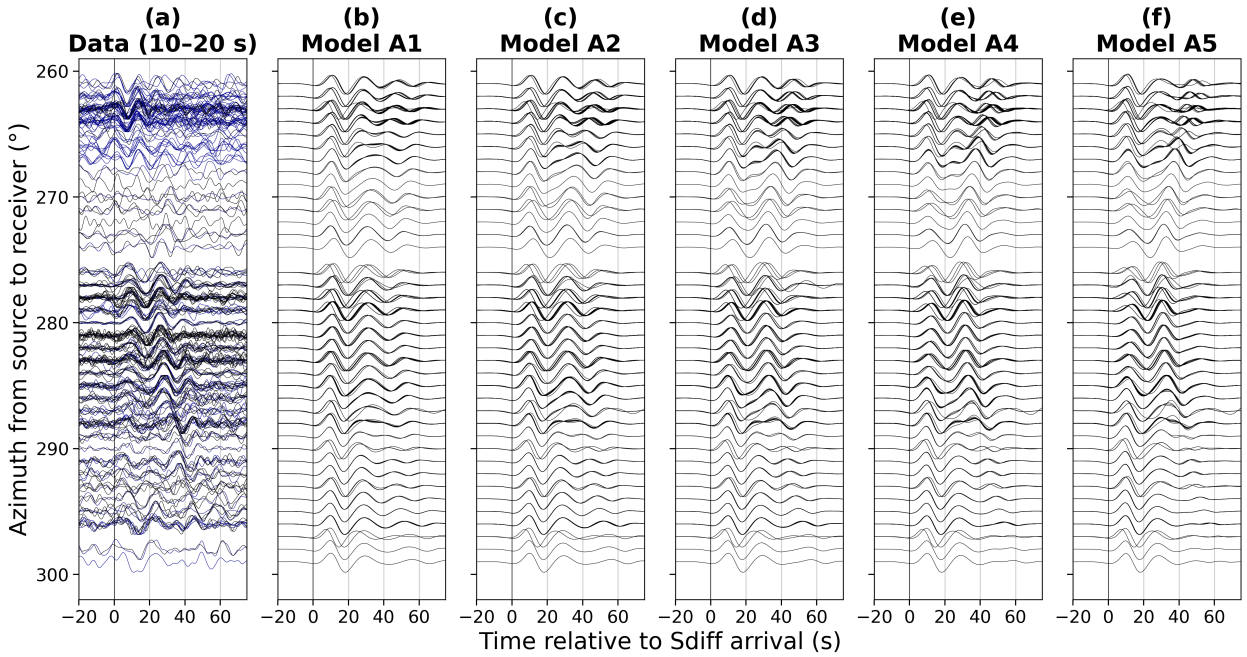

Figure S11. (a) Real data and (b-f) synthetic waveforms for PREM with a cylindrical ULVZ with parameters corresponding to Table S2. Model A parameters correspond to on the trade-off curve from the 2DWT inversion ensemble (white circles, Figure S7). Data are filtered between 10–20 s period.

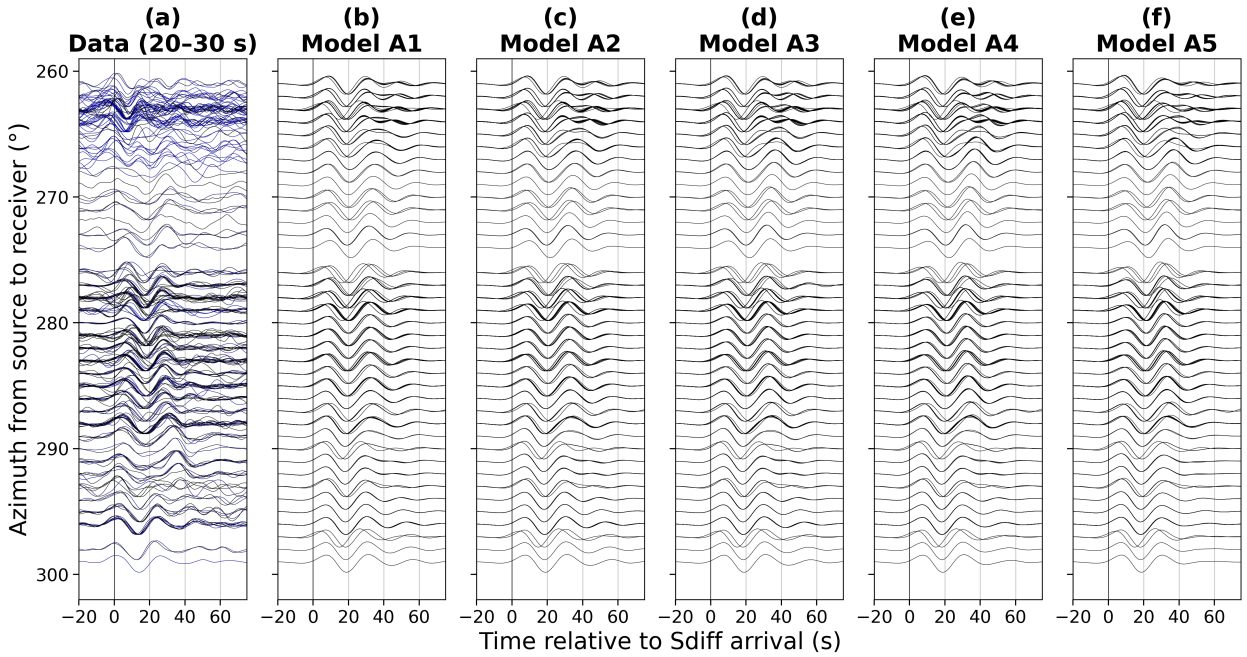

Figure S12. Same as Figure S11 but filtered between 20–30 s period.

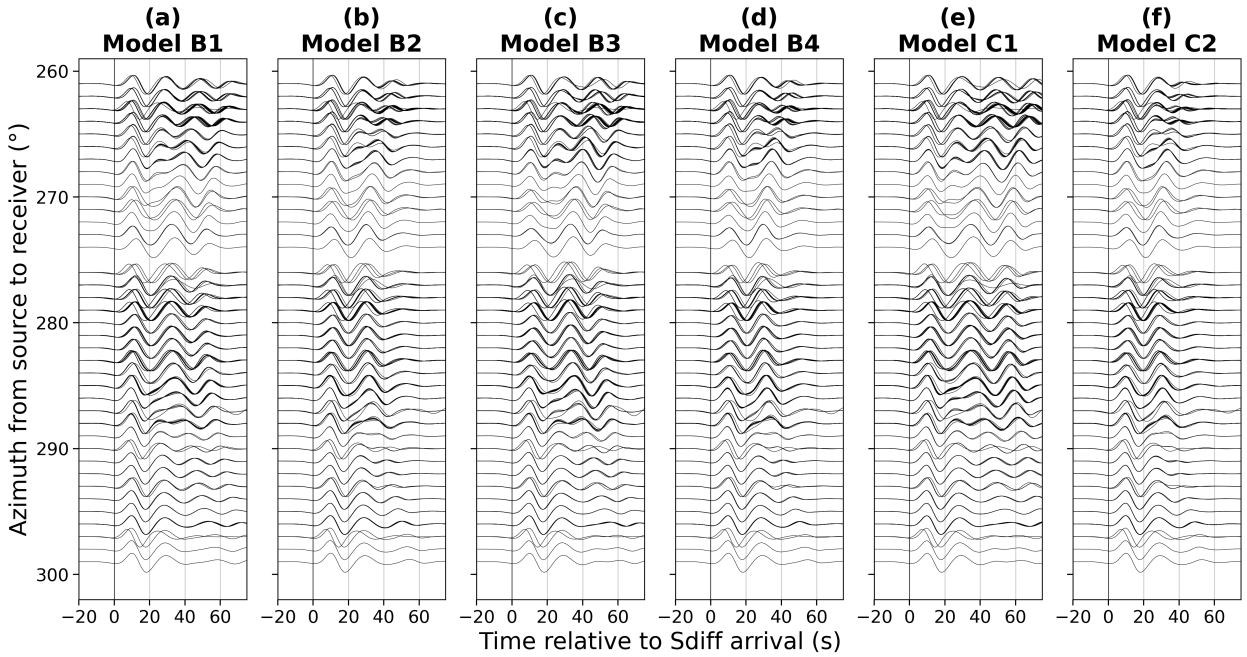

Figure S13. (a-f) Synthetic waveforms for PREM with a cylindrical ULVZ with parameters corresponding to Table S2. Model B & C parameters correspond to off the trade-off curve from the 2DWT inversion ensemble (grey and black circles in Figure S7, respectively). Data are filtered between 10–20 s period.

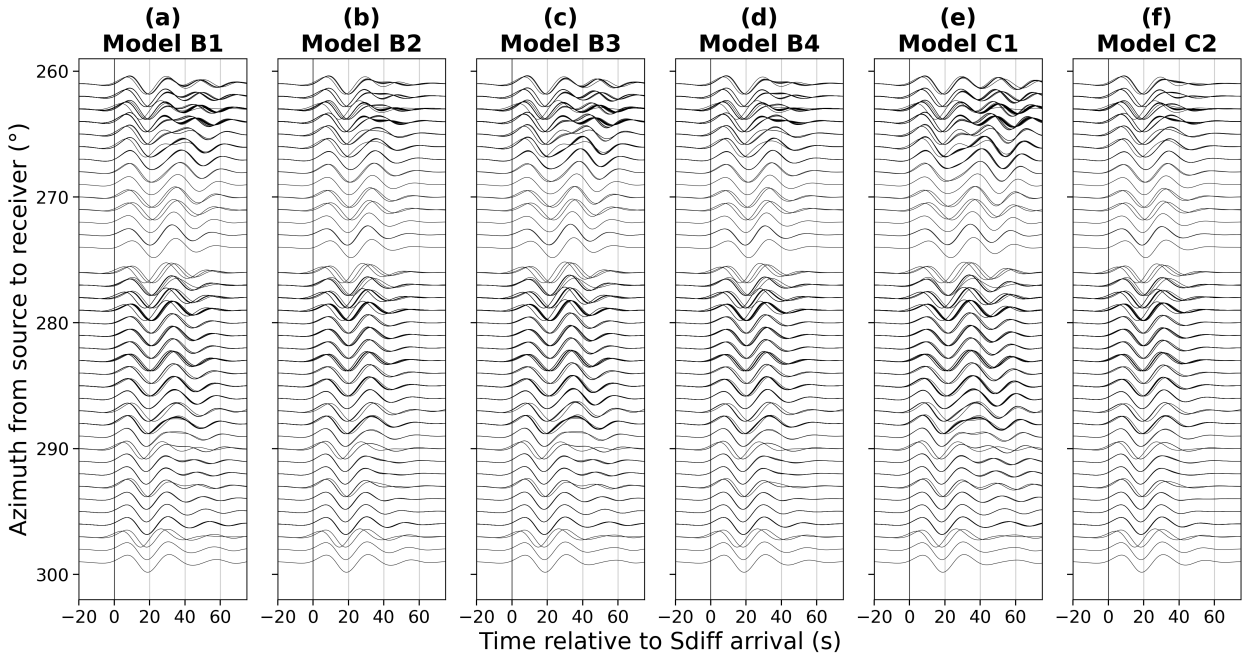

Figure S14. Same as Figure S13 but filtered between 20–30 s period.

S3 Waveform modelling of ULVZs in earlier studies

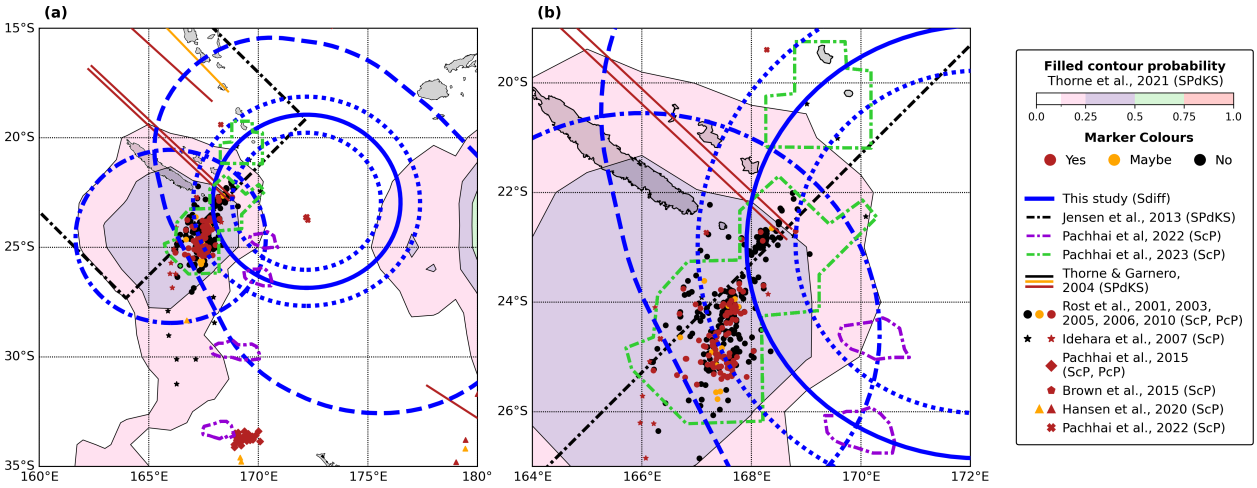

Figure S15. Figure 1 but modified and zoomed in. We use Model A3 as a proxy for the probability map local peak near to our mapping region relocated to 166° E and 24.5° S (blue dashdotted outline) for the synthetics shown in Figures 7 & S16. The uncertainty in the radius of the preferred model is shown as dotted blue lines; many bounce point lie within or near the upper limit of the radius.

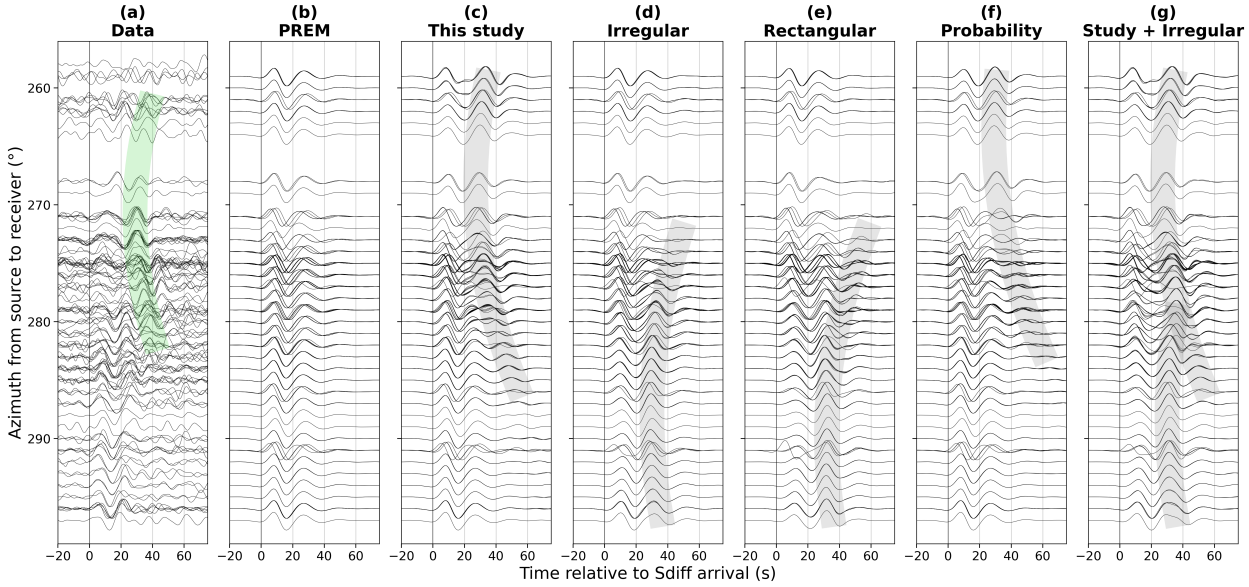

Figure S16. Same as Figure 7 but for Event 1, with an additional simulation (g) which includes both our preferred model of the Vanuatu ULVZ and the irregular model of the Samoa ULVZ implemented by Krier et al. [2021], equivalent to (c+d).

References

Ekström, G., Nettles, M. and Dziewonski, A. M. [2012], 'The global CMT project 2004-2010: Centroid-moment tensors for 13,017 earthquakes', *Physics of the Earth and Planetary Interiors* **200-201**, 1–9.

Krier, J., Thorne, M. S., Leng, K. and Nissen-Meyer, T. [2021], 'A compositional component to the Samoa ultralow-velocity zone revealed through 2-and 3-D waveform modeling of SKS and SKKS differential travel-times and amplitudes', *Journal of Geophysical Research: Solid Earth* **126**(7), e2021JB021897.

Okada, Y., Kasahara, K., Hori, S., Obara, K., Sekiguchi, S., Fujiwara, H. and Yamamoto, A. [2004], 'Recent progress of seismic observation networks in Japan—Hi-net, F-net, K-NET and KiK-net', *Earth, Planets and Space* **56**, xv–xxviii.